NeuroImage 249 (2022) 118872

Contents lists available at ScienceDirect

NeuroImage

journal homepage: www.elsevier.com/locate/neuroimage

# Charting human subcortical maturation across the adult lifespan with in vivo 7 T MRI

Steven Miletić[a,1,*], Pierre-Louis Bazin[a,b,1], Scott J.S. Isherwood[a], Max C. Keuken[a], Anneke Alkemade[a,1], Birte U. Forstmann[a,1,**]

[a] University of Amsterdam, Department of Psychology, Integrative Model-based Cognitive Neuroscience research unit (IMCN), Nieuwe Achtergracht 129B, Amsterdam 1001 NK, the Netherlands

[b] Max Planck Institute for Human Cognitive and Brain Sciences, Departments of Neurophysics and Neurology, Stephanstraße 1A, Leipzig, Germany

ARTICLE INFO

*Keywords:*
Subcortex
Morphometry
Iron
Myelin
Aging

ABSTRACT

The human subcortex comprises hundreds of unique structures. Subcortical functioning is crucial for behavior, and disrupted function is observed in common neurodegenerative diseases. Despite their importance, human subcortical structures continue to be difficult to study in vivo. Here we provide a detailed account of 17 prominent subcortical structures and ventricles, describing their approximate iron and myelin contents, morphometry, and their age-related changes across the normal adult lifespan. The results provide compelling insights into the heterogeneity and intricate age-related alterations of these structures. They also show that the locations of many structures shift across the lifespan, which is of direct relevance for the use of standard magnetic resonance imaging atlases. The results further our understanding of subcortical morphometry and neuroimaging properties, and of normal aging processes which ultimately can improve our understanding of neurodegeneration.

## 1. Introduction

The human subcortex comprises hundreds of unique structures (Alkemade et al., 2013; Forstmann et al., 2017) which receive interest from a broad range of neuroscientific disciplines (e.g. Lozano et al., 2019; Raznahan et al., 2014; Shepherd, 2013; Tian et al., 2020). Subcortical functioning is crucial for normal behavior and physiology including decision making (Ding and Gold, 2013), reward processing (O'Doherty et al., 2004; Schultz et al., 1997), and motor behavior (Mink, 1996). Disruption of subcortical structures is observed in common neurodegenerative diseases including Parkinson's (Hirsch et al., 1988) and Alzheimer's disease (Ehrenberg et al., 2017; German et al., 1987). Subcortical structures are also of interest as (potential) deep brain stimulation (DBS) targets in Parkinson's disease (Fasano and Lozano, 2015; Limousin et al., 1995) and other disorders such as major depression and epilepsy (Lozano et al., 2019).

Research into the subcortex depends on the imaging of individual subcortical structures. However, visualizing subcortical structures using in vivo methods such as magnetic resonance imaging (MRI) is challenging due to their close spatial proximity, biophysical properties, and morphometry (Keuken et al., 2018). As a consequence, our understanding of the subcortex remains limited, and lags behind our understanding of the cortex. Quantitative ultra-high field 7 Tesla MRI provides a method to overcome the challenges associated with visualizing subcortical structures (Bazin et al., 2020; Keuken et al., 2018), which we use here to provide a cross-sectional account of the subcortex across the adult lifespan.

The biophysical properties that determine the appearance of brain structures on MR images include the iron and myelin contents, which influence the main sources of contrast in MRI: the longitudinal and effective transverse relaxation rates, and the local susceptibility to magnetic fields. Furthermore, iron and myelin are highly biologically relevant: Myelin plays an important role in plasticity and development (e.g. Fields, 2015; Hill et al., 2018; Turner, 2019), and iron is crucial for normal tissue functioning (e.g. Zecca et al., 2004). Iron deposition (Daugherty and Raz, 2013; Hallgren and Sourander, 1958; Raz and Rodrigue, 2006; Ward et al., 2014; Zecca et al., 2004) and decreased myelination (Raz and Rodrigue, 2006; Shen et al., 2008) are part of normal aging processes, but excessive iron accumulation and myelin degradation are prominent in diseases including Parkinson's and Alzheimer's disease (e.g. Mancini et al., 2020; Zecca et al., 2004). A description of normal age-related changes in iron and myelin content can therefore

* Corresponding author.
** Co-corresponding author.
*E-mail addresses:* s.miletic@uva.nl (S. Miletić), buforstmann@gmail.com (B.U. Forstmann).
[1] Authors contributed equally.

https://doi.org/10.1016/j.neuroimage.2022.118872.
Received 19 July 2021; Received in revised form 20 December 2021; Accepted 3 January 2022
Available online 7 January 2022.

provide a frame of reference to contrast pathological iron accumulation and myelin degradation, and to refine methods for the early detection of pathological alterations using MRI measures as biomarkers.

An additional factor determining the appearance of the human subcortex is the small size of the individual structures. Prominent subcortical structures such as the subthalamic nucleus are as small as a few millimeters thick, limiting the number of voxels they encompass on MR images commonly used in research and in the clinic. Moreover, voxels at the border of structures likely include tissue from adjacent structures (partial voluming), which can lead to biases especially when voxel sizes are large relative to the structure (Mulder et al., 2019). Structure size should therefore be taken into account when imaging the subcortex. An important additional consideration here is the development of atrophy with increasing age, which is reflected in reduced volume of gray matter structures (Cherubini et al., 2009; Courchesne et al., 2000; Herting et al., 2018; Lemaitre et al., 2012; Raz, 2004; Raz and Rodrigue, 2006; Walhovd et al., 2005) and which results in more cerebrospinal fluid (CSF) and larger ventricles (Good et al., 2001; Greenberg et al., 2008; Stafford et al., 1988; Walhovd et al., 2005). In addition to volume changes, atrophy can result in a shift in the location of structures (Keuken et al., 2017; 2013; Kitajima et al., 2008).

These factors combined hamper visualization of the subcortex when using conventional MRI techniques. Furthermore, the age-related alterations in these factors alter the appearance of the subcortex with increasing age. In this study, we provide a detailed account of 17 subcortical structures and ventricles using data from 105 healthy participants across the adult lifespan obtained with in vivo methods tailored for studying the human subcortex (Alkemade et al., 2020a). For practical reasons, and without intending to make any claims on how a subcortical structure should be defined, we define subcortical as any anatomical structure located inferior to the corpus callosum.

Compared to previous studies, which often focus on a select set of regions and/or MRI or morphometry measures at a time, we simultaneously study a wider range of structures and measures. These include structures and measures that have not been studied before in the context of aging. The structures under investigation include gray matter regions, white matter tracts, and the ventricles. The inclusion of a variety of structures allows us to study across-region similarities and differences in aging effects. Similarly, the large set of quantitative MRI (qMRI) contrasts and morphometry measures allows us to explore aging as a multidimensional process. As such, we provide a wide picture of subcortical aging across metrics and regions.

Furthermore, we improve upon previous methods by using qMRI acquired at 7 Tesla (T) with 0.7 mm isotropic resolution, and employ the MASSP method (Bazin et al., 2020) to obtain automated delineations with an accuracy that approximates the gold standard of manual delineations (Alkemade et al., 2021; Bazin et al., 2020). Tullo et al. (2019) have shown that the choice of delineation method can influence which age-related change models provide best fits to empirical data, illustrating the importance of high-quality delineations in aging studies. Additional methodological improvements include the development of a subcortical thickness estimation method, which provides a thickness estimate analogous to cortical thickness metrics; as well as the development of iron and myelin approximation methods. Combined, these methods allow us to interpret our results in terms of the hypothesized biological processes that occur during aging: myelin degradation, iron accumulation, and atrophy (changes in size, shape, and location).

## 2. Methods

### 2.1. Participants

We used the Amsterdam ultra-high field adult lifespan database (AHEAD; Alkemade et al., 2020a), which consists of multimodal MRI data from 105 healthy participants. Inclusion criteria were age 18–80 years and self-reported health at the time of inclusion. A histogram depicting the distribution of ages in the sample is shown in Fig. S1. Exclusion criteria were any factors that could potentially interfere with MRI scanning, including MRI incompatibility (e.g., pacemakers), pregnancy, and self-reported claustrophobia. At least six males and females were included in each age decade to ensure full coverage of the adult lifespan. All participants gave written informed consent prior to the onset of data collection. The local ethics board approved the study.

### 2.2. MRI scanning

Images were acquired at the Spinoza Centre for Neuroimaging in Amsterdam, the Netherlands, using a Philips Achieva 7 T MRI scanner with a 32-channel phased-array coil. Routine quality checks of the quantitative maps appearance were performed previously (Alkemade et al., 2020a) and all subjects from the database were included for analysis. T1-weighted, T2* contrasts were obtained using a MP2RAGEME (multi-echo magnetization-prepared rapid gradient echo) sequence (Caan et al., 2019). The MP2RAGEME is an extension of the MP2RAGE sequence (Marques et al., 2010) and consists of two rapid gradient echo ($GRE_{1,2}$) images that are acquired in the sagittal plane after a 180 degrees inversion pulse and excitation pulses with inversion times $TI_{1,2}$ = [670 ms, 3675.4 ms]. A multi-echo readout was added to the second inversion at four echo times ($TE_1$= 3 ms, $TE_{2,1\text{-}4}$ = 3, 11.5, 19, 28.5 ms). Other scan parameters include flip angles $FA_{1,2}$ = [4, 4] degrees; $TR_{GRE1,2}$ = [6.2 ms, 31 ms]; bandwidth = 404.9 MHz; $TR_{MP2RAGE}$ = 6778 ms; acceleration factor SENSE PA = 2; FOV = 205 × 205 × 164 mm; acquired voxel size = 0.7 × 0.7 × 0.7 mm; acquisition matrix was 292 x 290; reconstructed voxel size = 0.64 × 0.64 × 0.7 mm; turbo factor (TFE) = 150 resulting in 176 shots; Total acquisition time = 19.53 min. No B1 field correction was performed; instead, the B1 field was optimized for subcortex during data acquisition.

### 2.3. Quantitative MRI modeling and parcellation

The MP2RAGEME consists of two interleaved MPRAGEs with different inversions and four echoes in the second inversion. Based on these images, we estimated quantitative MR parameters of R1, R2* and QSM as follows. First, we took advantage of the redundancy in the MP2RAGEME sequence to perform a PCA-based denoising with LCPCA (Bazin et al., 2019). R1 maps were then computed using the standard look-up table approach of Marques et al. (2010) to recover T1 values from the measured signals. R2*-maps were computed by least-squares fitting of the exponential signal decay over the four echoes of the second inversion. QSM images were obtained from the phase maps of the second, third, and fourth echoes of the second inversion with TGV-QSM (Langkammer et al., 2015). Skull stripping, required for QSM, was performed on the second inversion, first echo magnitude image (Bazin et al., 2014).

The anatomical regions of interest were defined with the MASSP automated algorithm (Bazin et al., 2020) on the basis of the R1, R2* and QSM image maps. The algorithm combines location, shape, and quantitative MRI priors to define 17 subcortical anatomical regions and ventricles, listed in Table 2. Separate masks for left and right hemisphere were obtained except for 3V, 4V, and *fx*.

For this study, the MASSP algorithm was trained on renormalized versions of the quantitative contrasts using a fuzzy C-means clustering of intensities, and linearly interpolating between cluster centroids (Pham and Bazin, 2009). The renormalized contrasts were thus less sensitive to the intensity variations induced by aging. Additionally, the registration to the MASSP atlas was performed in two successive steps, producing more accurate alignment of the anatomical priors with each subject. This second step was particularly important to compensate for the large variability of ventricular size and shape in the study cohort. The algorithm itself was unchanged, and we re-validated the accuracy of the method against manual delineations as in Bazin et al. (2020).

**Table 1**
Model comparisons for the iron (top) and myelin (bottom) approximation models. Bold face indicates the winning models, which have the lowest AIC and BIC values.

| | Parameterized model | $R^2$ | AIC | BIC |
|---|---|---|---|---|
| Iron | $y = 8.27718$ | 0.0 | 117.2952 | 118.1285 |
| | $y = -6.83576 + 0.33962 \times R2*$ | 0.9161 | 77.1614 | 78.8278 |
| | $y = -11.25376 + 29.28218 \times R1$ | 0.4811 | 108.1415 | 109.8079 |
| | $y = -3.45436 - 9.2427 \times R1 + 0.40217 \times R2*$ | 0.933 | 75.3461 | 77.8458 |
| | $y = 4.68168 + 274.40993 \times \mathrm{QSM}$ | 0.8107 | 90.9972 | 92.6637 |
| | $\mathbf{y = -3.82834 + 0.2431 \times R2* + 98.27947 \times QSM}$ | **0.9461** | **71.6371** | **74.1368** |
| | $y = -2.59147 + 11.83574 \times R1 + 227.0019 \times \mathrm{QSM}$ | 0.8651 | 87.2357 | 89.7354 |
| | $y = -2.41386 - 5.22683 \times R1 + 0.29445 \times R2* + 82.01402 \times \mathrm{QSM}$ | 0.9507 | 72.1302 | 75.463 |
| Myelin | $y = 9.34013$ | 0.0 | 78.8674 | 79.4324 |
| | $y = 4.41227 + 0.09621 \times R2*$ | 0.2178 | 77.6741 | 78.804 |
| | $y = -6.25936 + 21.5651 \times R1$ | 0.7746 | 61.4997 | 62.6296 |
| | $\mathbf{y = -7.98965 + 31.87483 \times R1 - 0.11182 \times R2*}$ | **0.8918** | **53.963** | **55.6579** |
| | $y = 8.80294 + 25.38923 \times \mathrm{QSM}$ | 0.0211 | 80.5908 | 81.7207 |
| | $y = -0.24058 + 0.25117 \times R2* - 155.23593 \times \mathrm{QSM}$ | 0.4399 | 75.3327 | 77.0276 |
| | $y = -7.7523 + 25.33129 \times R1 - 58.19931 \times \mathrm{QSM}$ | 0.8616 | 57.1586 | 58.8535 |
| | $y = -7.97876 + 32.10295 \times R1 - 0.11662 \times R2* + 3.32451 \times \mathrm{QSM}$ | 0.8918 | 55.9549 | 58.2147 |

**Table 2**
Regions of interest. Midline structures were parcellated as a single structure, all other structures (indicated by bold-faced letters) were parcellated separately per hemisphere. Abbreviations in italics indicate white matter structures.

| | |
|---|---|
| **AMG**: Amygdala | **SN**: Substantia nigra |
| **CL**: Claustrum | **STN**: Subthalamic nucleus |
| *fx*: Fornix | **STR**: Striatum |
| **GPe**: Globus Pallidus Externa | **THA**: Thalamus |
| **GPi**: Globus Pallidus Interna | **VTA**: Ventral Tegmental Area |
| ***ic***: Internal Capsule | **LV**: Lateral ventricle |
| **PAG**: Periaqueductal gray | 3V: Third ventricle |
| **PPN**: Pedunculopontine nucleus | 4V: Fourth ventricle |
| **RN**: Red nucleus | |

Improvements were noticeable for more variable structures such as the ventricles, fornix, and claustrum, as well as some of the more challenging smaller structures, see Fig. S2.

### 2.4. Iron and myelin approximation

Iron and myelin are main determinants of MR image contrast (Stüber et al., 2014). Several lines of research indicate that the concentrations of iron and myelin are approximately linearly related to qMRI metrics R1, R2* and QSM (Hametner et al., 2018; Mangeat et al., 2015; Marques et al., 2017; Metere and Möller, 2018; Rooney et al., 2007; Stüber et al., 2014). Whereas many studies make inferences on iron and myelin contents based on a single MRI modality (e.g., Daugherty and Raz, 2013; Khattar et al., 2021), we use the multimodal quantitative nature of our data to estimate the relation between multiple modalities and iron and myelin. Assuming a linear relationship between iron and myelin on the one hand, and qMRI on the other, linear models can be fit and used to predict iron and myelin contents based on qMRI values (Metere and Möller, 2018):

$$\begin{aligned} Iron &= Intercept + w_{i,qsm} * QSM + w_{i,R2^*} * R2^* + w_{i,R1} * R1 \\ Myelin &= Intercept + w_{m,qsm} * QSM + w_{m,R2^*} * R2^* + w_{m,R1} * R1 \end{aligned} \quad (1)$$

Estimating the parameters $w$ of these models requires population-average estimates of iron and myelin content for a variety of regions of interest that cover the range of R1, R2*, and QSM values observed across the brain. Following the approach by Metere and Möller (2018), we obtained these values from the literature (Hallgren and Sourander, 1958; Metere and Möller, 2018; Randall, 1938), and supplemented those values using observations in *post mortem* tissue (detailed below). For iron estimates, Hallgren and Sourander (1958) provided quantifications across a number of subcortical and cortical regions, which, combined with the corresponding qMRI values obtained using our own MRI data, allowed for stable estimators of the weights in Eq. (1). An iron concentration of 0.061 in the ventricles was assumed (following Metere and Möller, 2018, who based this value on LeVine et al., 1998).

As a reference for myelin concentrations, we used work by Randall (1938), which provides lipid concentrations for the corona radiata, frontal and parietal white matter, brain stem, thalamus, caudate, and frontal and parietal gray matter. Following Metere and Möller (2018), we assumed that these lipid concentrations reflect myelin concentrations. Unfortunately, the reported regions do not include iron-rich nuclei, which limits the range of (especially) R2* and QSM values with known corresponding lipid concentrations. Using a limited number of regions of interest to estimate the myelin model could limit the generalizability of the estimated parameters to structures with lower R2* and/or QSM values, which would bias myelin estimates in iron-rich structures like some basal ganglia nodes (e.g., based on using only Randall's (1938) lipid concentrations, Metere and Möller (2018) obtained *negative* myelin concentrations in various basal ganglia structures).

To supplement the literature-based myelin concentrations, we approximated the myelin contents of other regions of interest using a *post mortem* specimen. Specifically, we used specimen #7 from Alkemade et al. (2020b), which was a 75 year old female, non-demented control. At the time the current experiments were performed, this was the only specimen fully processed. Here, we made the following assumptions:

1. The optic density of tissue in our silver stains is approximately linearly related to the concentration of myelin in that tissue in our regions of interest (see Fig. 1). Here, we confirmed that silver stains were not saturated even in the white matter regions;
2. The myelin concentrations in the *post mortem* specimen do not show gross abnormalities. We found no indications that our *post mortem* specimen showed major abnormalities in myelin properties. We confirmed that the donor had no clinical record of neurodegenerative disease, a diagnosis that was confirmed *post mortem* by a board-certified neuropathologist;
3. The myelin concentrations in white matter reported by Randall (1938) are in the same range of the myelin concentration in the internal capsule. Similarly, the myelin concentrations in parietal cortex are in the same range of the concentrations in insular cortex.

Seven 200 μm coronal sections of a single specimen were stained according to the method described by Bielschowsky (for details, see Alkemade et al., 2020b). Sections included the caudate nucleus, thalamus, internal capsule, and insular cortex, in which we estimated the median intensity of the lightness of the stain (the optic density).

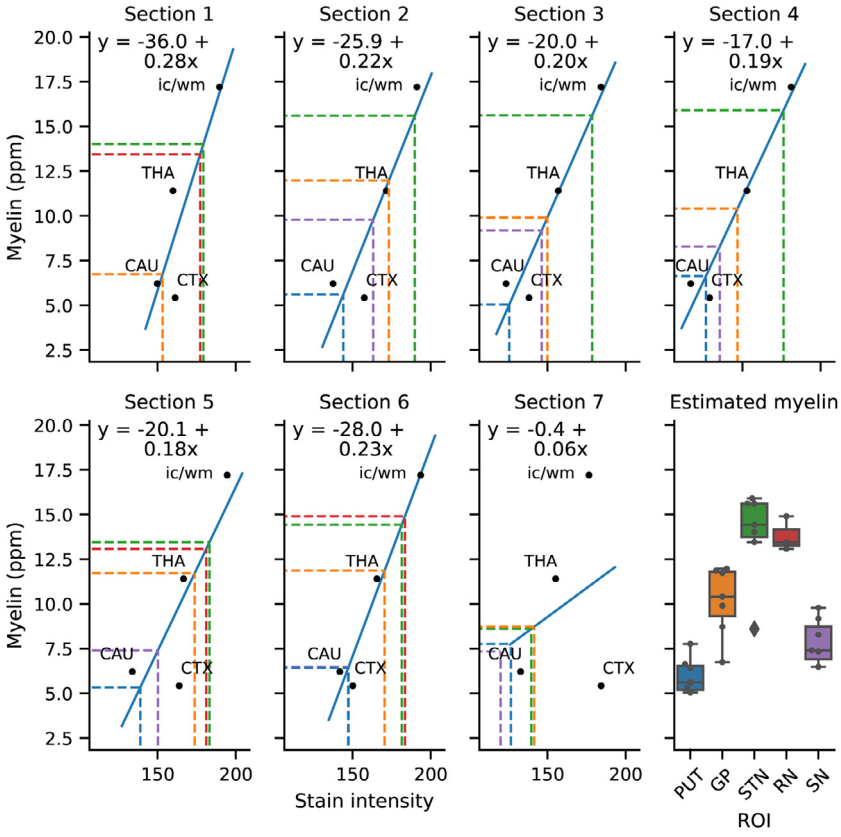


**Fig. 1.** Procedure of estimating myelin contents using a *post mortem* specimen. In each section (seven in total), the stain intensities corresponding to CAU, THA, insular cortex (CTX) and the internal capsule (ic/wm) were estimated. For each section individually, a calibration curve was estimated to map stain intensity to myelin values (solid blue lines and equations). Within the range of interest, the relation between stain intensity and myelin content could be approximated with a linear trend. Then, within each section separately, the intensity values for putamen (PUT), GP, STN, RN, and SN were estimated (colored dashed lines; note that not all sections contained all structures), and the corresponding myelin values were calculated. Per region, the median estimate (across sections) was used as a final estimate. Boxplots in the right panel show across-section variability in estimated myelin contents and suggest agreement across sections. The center line in each box marks the median, box limits are the across-section interquartile range, and whiskers are at 1.5 times the interquartile range below and above the box limits. ROI = Region of interest. (For interpretation of the references to color in this figure legend, the reader is referred to the web version of this article.)

Randall (1938) reports quantified lipid concentrations of the caudate nucleus and thalamus, which can be directly compared to the stain intensities, as well as of parietal gray and white matter. The caudate nucleus, thalamus, and parietal gray and white matter (as reported by Randall (1938)) were not visible in the same histological section, and we therefore used insular cortex as a reference region for gray matter, and the internal capsule as a reference region for white matter. For each section separately, we then created a linear calibration curve, which allowed us to determine lipid concentrations based on the stain intensity (Fig. 1) for putamen, globus pallidus, subthalamic nucleus, red nucleus, and substantia nigra.

For the region of which population-averaged iron and myelin contents were known, we estimated the qMRI values using the MRI data. Median qMRI values were calculated using the MASSP masks for subcortical regions, and a MGDM and CRUISE parcellation was used to obtain individual masks for brain stem, cerebellum, and cortex (Bazin et al., 2014). We included only participants of 30 years and older to match the ages of the specimens on which the iron and myelin estimates are based. For brain regions for which we had estimated the myelin content using our *post mortem* specimen, we only included AHEAD subjects of 70 years and older (17 participants total) to approximately match ages of the MRI data and the specimen. Tables S1 and S2 list the iron and myelin concentrations, respectively, and their corresponding qMRI values, that were used to estimate the parameters in Eq. (1).

To test whether all qMRI metrics were required as predictors to accurately predict iron and myelin content, we fitted linear models with all eight possible combinations of R1, R2*, and QSM. Models were fitted using ordinary least squares (OLS). For each model, we estimated the Akaike information criterion (AIC; Akaike, 1973) to identify the model that is expected to have the highest predictive performance, and used the model with lowest AIC values (AIC and BIC values agreed on the winning model). We used the AIC here instead of the BIC as the AIC is expected to select models with the highest cross-validated predictive performance, whereas the BIC is expected to select the data-generating model (Wagenmakers and Farrell, 2004). The model comparisons, including the parameterized winning models, can be found in Table 1.

Comparisons of the explained variance ($R^2$) of the individual models show that, when relying on single qMRI metrics, R2* explained most variance in iron (91.6%), followed by QSM (81.1%). Combining R2* and QSM increased the explained variance to 94.6%, which implies R2* and QSM largely (but not only) explain the same variance in iron. Nonetheless, the increase in variance explained acquired by adding QSM to the R2* model was sufficient to warrant the additional model complexity, as evidenced by the lower AIC and BIC values.

As expected, R1 explained most variance in myelin (77.4%), while R2* explained only limited variance in myelin (21.78%, only marginally better than an intercept-only model). However, the combination of R1 and R2* explained 89.2% of variance, suggesting R1 and R2* do not largely explain the same variance in myelin, but each explain unique proportions. AIC and BIC values preferred the model that included both R1 and R2* as predictors.

Fig. 2 visualizes quality of fit of the winning models. Note that the model weights cannot directly be compared to the weights from Stüber et al. (2014), which were obtained using formalin fixated *post mortem* tissue. Formalin fixation can change qMRI values (Birkl et al., 2016; Langkammer et al., 2012; Schmierer et al., 2008; Shepherd et al., 2009; Tovi and Ericsson, 1992). A second complicating factor is that qMRI values can vary between MRI sites (Mancini et al., 2020), suggesting the need to re-estimate model weights when using qMRI obtained at a different site.

Using these simplified biophysical models, we calculated whole-brain iron and myelin maps, and obtained participant-specific myelin and iron values for all structures using the MASSP masks. Iron and myelin maps of a representative participant are shown in Fig. 3. To confirm our models are able to reproduce the between-region variability in iron and myelin that has been reported in the literature, we com-

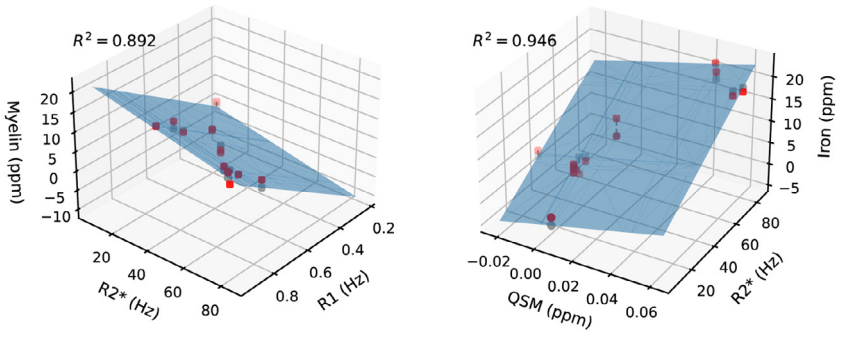


**Fig. 2.** Quality of fit of the myelin (left) and iron (right) model. The planes are given by the winning models in Table 1. Red dots illustrate data points, gray dots are the model predictions for these data points. (For interpretation of the references to color in this figure legend, the reader is referred to the web version of this article.)

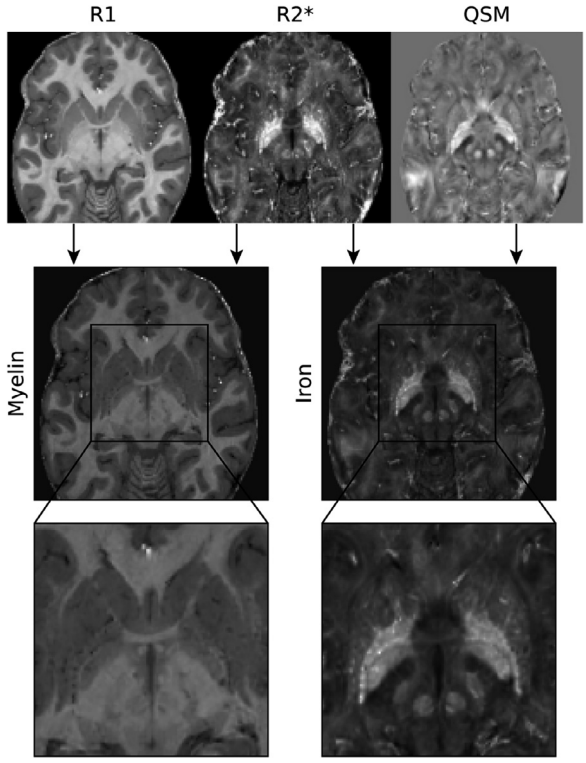


**Fig. 3.** Example of myelin (left) and iron map (right) of a representative participant. The top row shows the R1, R2*, and QSM maps, which were linearly combined into myelin and iron maps (middle and bottom row) using the winning models detailed in Table 1. Note the hyperintense appearance of iron rich structures such as the rounded shape of the red nucleus. (For interpretation of the references to color in this figure legend, the reader is referred to the web version of this article.)

pared the myelin and iron predictions to the concentrations in the literature (Fig. 4). We also compared the myelin predictions to the myelin concentrations estimated based on the *post mortem* tissue. These comparisons suggest reasonable correspondence between literature-derived and qMRI-derived iron and myelin concentrations for most regions, but not all. Regions with relatively large discrepancies include the brainstem, which might arise due to the fact that the iron literature reported concentrations in the medulla oblongata, whereas the qMRI data delineation included the entire brainstem. Similarly, the iron literature provided separate estimates for the putamen and caudate, whereas the qMRI delineations included the striatum as a single region, and as such the qMRI-derived iron concentrations cannot recover any differences between the putamen and caudate. Finally, the qMRI-derived myelin estimates are higher than the *post mortem* estimates, which might be related to neuromelanin, as this results in a lower intensity in the *post mortem* tissue, potentially resulting in a negative bias in the corresponding myelin estimate.

It is important to emphasize that the iron and myelin estimates we report are based on simplifying assumptions with regard to the linearity of the relation between qMRI and iron/myelin, and on the iron/myelin concentrations on which the biophysical models are fitted (detailed above). As such, the iron and myelin estimates should be not be interpreted as absolute measurements, but rather as approximations that serve to guide the interpretations of qMRI values in terms of the most likely underlying biological contributors to those values.

### 2.5. Thickness estimation

We calculated local structure thickness based on a medial skeleton representation: for each structure, we estimated the skeleton as the ridge equidistant to the structure boundaries. Thickness was defined as twice the distance between the skeleton and the closest boundary, using the method described in Bazin et al. (2020). In other words, local thickness measures at every location inside the structure the distance between the two closest boundaries of that structure, extending the concept of cortical thickness to more complex shapes. Contrary to volume, thickness can be determined at the position of each voxel within a structure, thus providing local information. A similar thickness measure was also used in Ho et al. (2020) to detect subtle shape differences.

### 2.6. Center of mass

For all structures, we calculated the center of masses in Cartesian x, y, and z coordinates per participant after an affine transformation to group space by aligning each subject to the MNI template with ANTs (Avants et al., 2008) using mutual information. The affine transformation was necessary to define a common space in which to compare structure location between subjects. It was preferred over a rigid or a nonlinear transformation in order to correct for inter-individual differences in intracranial volume and neurocranium shape, while retaining inter-individual variability in anatomy relative to the neurocranium.

### 2.7. Age-related change modeling

We describe the age-related changes in iron concentration, myelin content, volume, and thickness, as well as in the center of mass in x, y and z coordinates. For iron, myelin and thickness, we report both a median reflecting the central tendency and interquartile range reflecting structure homogeneity. For thickness, the interquartile range reflects the within-structure variability of thickness, quantifying the regularity of the shape. We also analyzed the R1, R2*, and QSM values, which can be found in the online app (https://subcortex.eu/app).

Exploratory modeling of the between-hemisphere differences per structure suggested no between-hemisphere difference in aging patterns for most structures. Therefore, we subsequently assumed that the age-related changes in each structure were the same in both hemispheres,

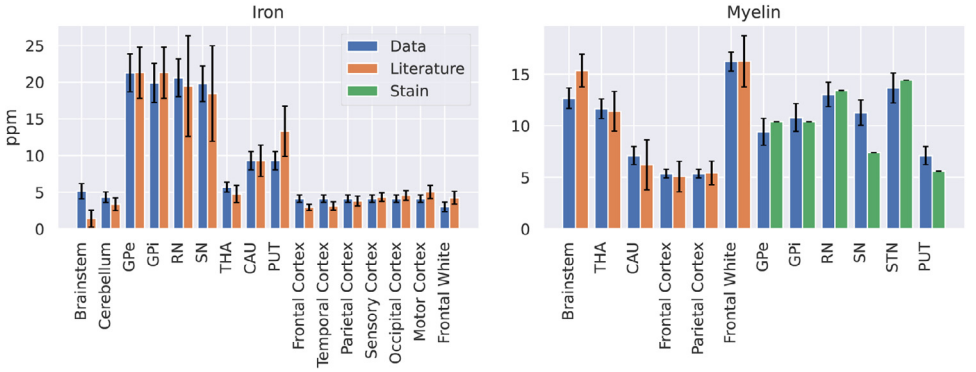


**Fig. 4.** Comparison between qMRI-derived iron (left) and myelin (right) values in our data and values reported in the literature. For myelin, we also compare the qMRI-derived estimates to the estimates in the *post mortem* tissue. Error bars indicate standard deviations. No error bars are present for the bars representing *post mortem* tissue, as these come from a single brain.

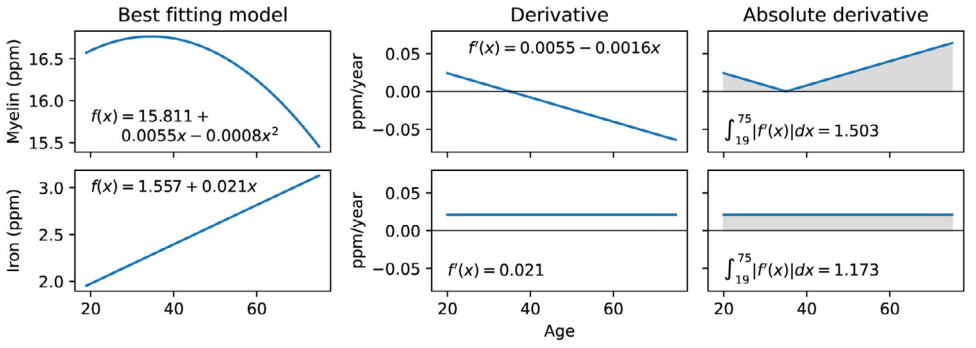


**Fig. 5.** Procedure of estimating total amount of change across the adult lifespan. The left column shows two example models: One inverted U-shape (median myelin change in the internal capsule), and one linear increase (median iron change in the amygdala). Formally, change across ages is given by the first derivative (middle column). To collapse over the direction of change (increase or decrease), we took the absolute of the derivative (right column). The sum of this absolute derivative (illustrated by the gray area under the curve) represents the total amount of change in a region. As a final step (not illustrated), the sum of the absolute derivative is divided by the model prediction at 19 years old, which represents the total amount of change relative to the baseline value.

to reduce the total number of models fitted. We collapsed across hemispheres by taking the mean value across both hemispheres per structure and participant.

Prior to fitting the aging models, we excluded outliers based on their Mahalanobis distance (cut-off 10.827, corresponding to $p < 0.001$, 0.69% of all data points). Per ROI and dependent variable, we then fit the following set of 24 potential models, with all possible combinations of the following predictors: A linear influence of age, a quadratic influence of age, sex, an interaction between age and sex, and an interaction between a quadratic influence of age and sex. We excluded models with both interaction terms, as this would imply implausibly large between-sex differences in aging patterns.

Models were fit with OLS as implemented in statsmodels (Seabold and Perktold, 2010) for the Python programming language. Models were compared with the Bayesian Information Criterion (BIC; Schwarz, 1978), which quantifies the quality of fit penalized for model complexity. Lower BIC values indicate more parsimonious trade-offs between quality of fit and model complexity and are preferred. Based on the winning model, we removed influential data points using Cook's distance (cut-off 0.2, 0.18% of all data points; we used a more conservative cut-off than $4/n$, which is sometimes recommended Rawlings et al., 1998). We then refitted all models on the data excluding the influential data points, and performed a new model comparison.

Using the winning age-related change models, we quantified the total age-related change. Fig. 5 illustrates the procedure to estimate this value, which involves taking the first derivative of the winning model (which quantifies the mean amount of change on every year), then taking the absolute (which quantifies the amount of change, irrespective of the direction of change), and then integrating over the age range of 19 to 75 years old. By integrating over the absolute derivative, age-related decreases and increases in a metric do not cancel out, but both count as 'change' and sum up across the range of the adult lifespan. To retain the mean direction of change in the metric, we took the negative of the total age-related change when the model's predicted value at 75 was lower than at 19.

The age range under consideration was limited to 75 because our data contains only one data point older than 75. Extrapolation of fitted regression models to beyond the range of the original data can lead to biases (e.g., Hahn, 1977), and since our data only contains one data point older than 75, we deemed it more conservative to restrict our inferences to the maximum of 75 years old. For winning models that included sex (or interactions between age and sex) as a predictor, the total age-related changes were calculated for both sexes separately and then averaged. Finally, we divided the total age-related change by the model's predicted value at 19 years old, in order to quantify the total age-related change relative to a baseline value.

### 2.8. Confidence intervals and standard errors

Confidence intervals in Fig. 6 were obtained using a bootstrapping procedure with 10,000 iterations. We iteratively sampled 105 random observations with replacement from the data, based on which we estimated the median, and took the 2.5th and 97.5th percentile of the 10,000 medians as the 95% confidence interval. The standard errors in Fig. S5 were obtained using a similar bootstrapping procedure, in which winning model specifications were iteratively fit on 10,000 random samples (drawn with replacement) from the data. Per iteration, the total age-related change metrics were estimated. The standard deviation of the total age-related change metrics across iterations was used as an estimator of the standard error. For winning models that do not include age as a predictor variable, the standard error is 0 since the total age-related change metric is 0 in each iteration.

## 3. Results

One hundred and five healthy volunteers were scanned using an ultra-high field 7 Tesla MRI scanner as part of the openly available

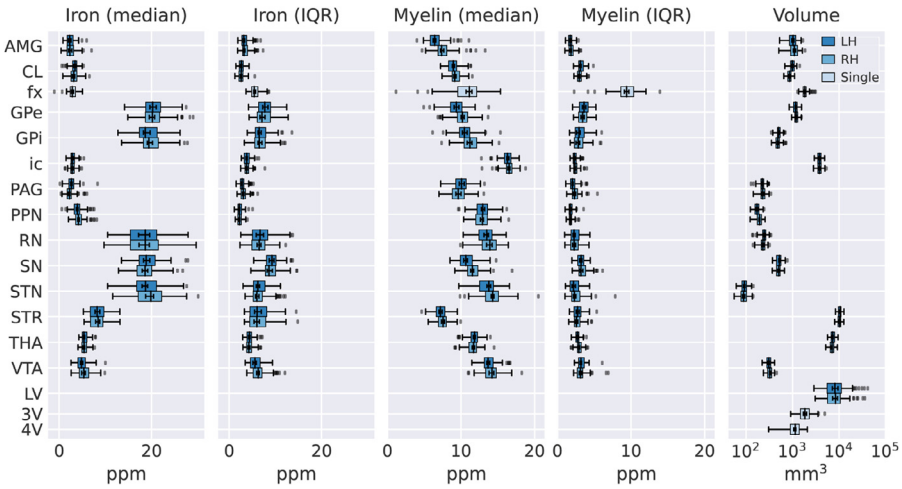


**Fig. 6.** Across-participant distributions of within-structure median and IQR of iron and myelin, and volumes per structure. The center line in each box marks the median, box limits are the across-participant IQR, and whiskers are at 1.5 times the IQR below and above the box limits. Error bars drawn inside boxes indicate 95% confidence intervals around the median, obtained by bootstrapping with 10,000 iterations. Colors indicate hemisphere (LH = left hemisphere, RH = right hemisphere, Single = structures that are continuous across the hemispheres), ppm = parts per million, mm = millimeter.

Amsterdam ultra-high field adult lifespan database project (AHEAD; Alkemade et al., 2020a). A quantitative, multi-modal MP2RAGE-ME sequence (Caan et al., 2019) with 0.7 mm isotropic resolution was used to simultaneously estimate R1, R2* and quantified susceptibility mapping (QSM) values in a single scanning sequence. For each participant, 17 subcortical structures and ventricles (see Table 2) were delineated using the Multi-contrast Anatomical Subcortical Structures Parcellation method (MASSP; Bazin et al., 2020).

We analyzed each structure by first estimating the iron and myelin concentrations, using simplified biophysical models that translate the measured R1, R2*, and QSM values into the most likely corresponding iron and myelin concentrations (see Methods). Note that these concentrations are approximations and do not reflect measured myelin and iron concentrations (see Limitations section). We obtained both the (within-structure) median of iron and myelin distributions, and the interquartile range (IQR) which reflects image noise and tissue (in)homogeneity. Second, we analyzed the structure morphometry by estimating volume and thickness. Thickness is defined as twice the distance between the boundary and the internal skeleton of the structure. As a local measure (contrary to volume), it is defined for every voxel in a structure, and it depends on the structure's shape. Also for thickness, we determined both the median and IQR, the latter reflecting the regularity of the structure's shape: Regularly shaped structures (e.g., the red nucleus) have a similar thickness at each voxel's location, resulting in lower between-voxel IQRs compared to complex shaped structures (e.g., the striatum). Third, we determined the location (center of mass in 3 Cartesian coordinates) of each structure. Center of mass was determined after applying an affine transformation to a group template, to account for inter-individual differences in intracranial volume and shape, while retaining inter-individual variability in distances relative to the neurocranium.

The distributions of iron, myelin, and volumes revealed a large between-structure heterogeneity in the human subcortex (Fig. 6). The globus pallidus externa and interna, red nucleus, substantia nigra, and subthalamic nucleus displayed the highest iron concentrations (both median and IQR), corroborating earlier reports (Haacke et al., 2005; Hallgren and Sourander, 1958; Ramos et al., 2014). In line with expectations, low iron concentrations in combination with high myelin concentrations were observed in the white matter structures under study: the internal capsule and the fornix. The estimated myelin concentrations of the subthalamic nucleus, red nucleus, and ventral tegmental area were relatively high, which causes the limited visibility of these structures on T1-weighted images (Keuken et al., 2018). For comparison, the estimated myelin concentrations of the striatum and amygdala were substantially lower, resulting in intensities comparable to cortical gray matter on T1-weighted images.

The within-structure IQR of iron scaled with the median estimates. This was the case across participants in all individual structures except for the left claustrum and left periaqueductal gray (lowest significant Pearson's correlation coefficient = 0.206 in the right claustrum; highest correlation coefficient = 0.876 in left striatum; all significant after correction for the false discovery rate at $q < 0.05$), as well as for the median and IQR of iron across structures ($r = 0.827$, $t(26) = 7.35$, $p < 0.001$).

Across subjects, the IQR of myelin decreased with increasing median myelin concentrations for all regions except the left pedunculopontine nucleus, right substantia nigra, left amygdala, both claustrums, right internal capsule, and fornix (significant correlation coefficients varied between −0.2183 for the left VTA and −0.58 for the right periaqueductal gray; all significant after correction for the false discovery rate at $q < 0.05$). Across regions, however, no correlation was observed between the median and IQR of myelin. The fornix had a particularly high IQR of myelin. This could potentially have been caused by partial voluming with the lateral ventricles, decreasing the myelin estimates at voxels near the boundary of the fornix.

### 3.1. Maturation effects

We next studied the age-related alterations in iron, myelin, and morphometry across the adult lifespan. We fit a set of 24 regression model specifications (with, as predictor variables, linear and/or quadratic effects of age, plus sex and potential interactions between sex and age) for all structures and measures individually. As we had no *a priori* hypothesis on lateralization, we collapsed across hemispheres to reduce the total number of fitted models. The model specification that showed the most parsimonious trade-off between quality of fit and model complexity (as quantified using the Bayesian information criterion; Schwarz (1978)) was considered the winning model and used for further analyses. To help navigate the winning models of each structure and measure (including R1, R2*, and QSM values), we developed an online interactive app, which is accessible at https://subcortex.eu/app (see also Fig. S4). Next to in the online app, all winning models (including the parameterization) can also be found in Figs. S6–S12.

We observed (median) iron accumulation in all structures except for the claustrum, globus pallidus interna, and periaqueductal gray, which instead showed stable iron concentrations (Fig. 7). With the exception of the globus pallidus interna, the iron-rich basal ganglia appeared to accumulate most iron during aging in absolute terms. The IQRs increased with age for all structures, revealing a global decrease in structure homogeneity. Since this decrease in homogeneity was also present in the structures where no median iron increase was observed, it likely partially reflects an increase in image noise. However, the increases in IQR were

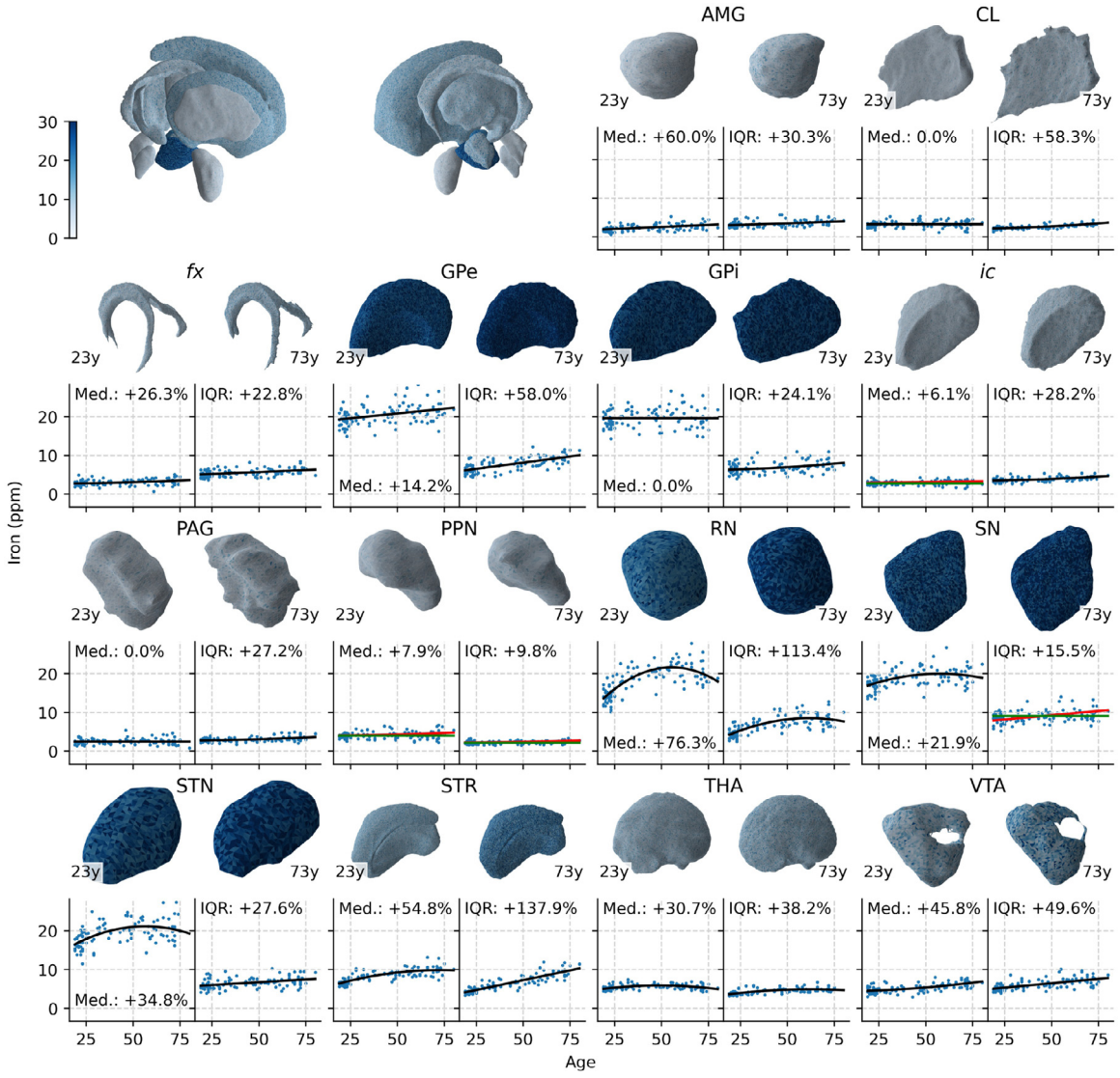


**Fig. 7.** Age-related changes in iron content. The meshes are based on the young (18–30 years old, mean 23; left) and elderly (70–80 years old, mean 73; right) participants after a non-linear transformation to MNI2009b space. Mesh colors illustrate the model predictions for the median and IQR of iron distributions at 23 (left) and 73 (right) years old, corresponding to the mean ages of the participant groups on which the meshes were based. Colors in the top-left meshes of all structures indicate model predictions at 23 years old. In case the winning model did not include sex as a predictor variable, the model predictions are shown in black lines; otherwise, green and orange lines are used for the predictions for women and men, respectively. The total amount of change in median (Med.) and IQR are shown in each scatterplot. The ventricles are assumed to have no iron and are excluded from this graph. (For interpretation of the references to color in this figure legend, the reader is referred to the web version of this article.)

higher in the structures that accumulate most iron (correlation between median and IQR iron increases across structure $r = 0.598$, $t(12) = 2.584$, $p = 0.024$, two-sided), suggesting that the (median) iron accumulation for these structures was not homogeneously distributed within the structure. This decrease in homogeneity was particularly strong in striatum and the red nucleus.

In line with expectations, we observed a general myelin degradation (see Fig. 8), except for in the amygdala, claustrum, and substantia nigra, where no alterations in myelin concentrations were detected. The largest (absolute) reduction of myelin was present in the fornix; the other white matter structure, internal capsule, showed a smaller decrease in myelin. The globus pallidus interna, periaqueductal gray, pedunculopontine nucleus, substantia nigra, and ventral tegmental area showed slightly higher median myelin concentrations in females than in males. Like in the case of iron, the increases in IQR of myelin reflected a trend of decreasing structure homogeneity across structures. Since these IQR increases were present for structures that did not show any change in median myelin content, they likely partially reflect increases in image noise.

Next, we analyzed the effects of atrophy (Fig. 9). The lateral and third ventricle showed a substantial volume increase with age, which can at least partially be explained by the filling of the intracranial space created by atrophied brain tissue. Contrary to expectations, the volume of the fourth ventricle decreased rather than increased. Inspection of the mesh of the fourth ventricle in the elderly suggests this may be caused by shrinkage of the superior part. Volume decreases were also found in the striatum, thalamus, amygdala, ventral tegmental area, periaqueductal gray, pedunculopontine nucleus, and red nucleus, likely reflecting atrophy. The internal capsule, fornix and globus pallidus interna showed a small increase in volume with age, suggesting white matter swelling, which could be caused by neuroinflammatory processes.

Atrophy of specific subparts of a structure, as a result of increased vulnerability to atrophy in that part, could result in shape changes (Ho et al., 2020; Raznahan et al., 2014). Shape changes can be detected by

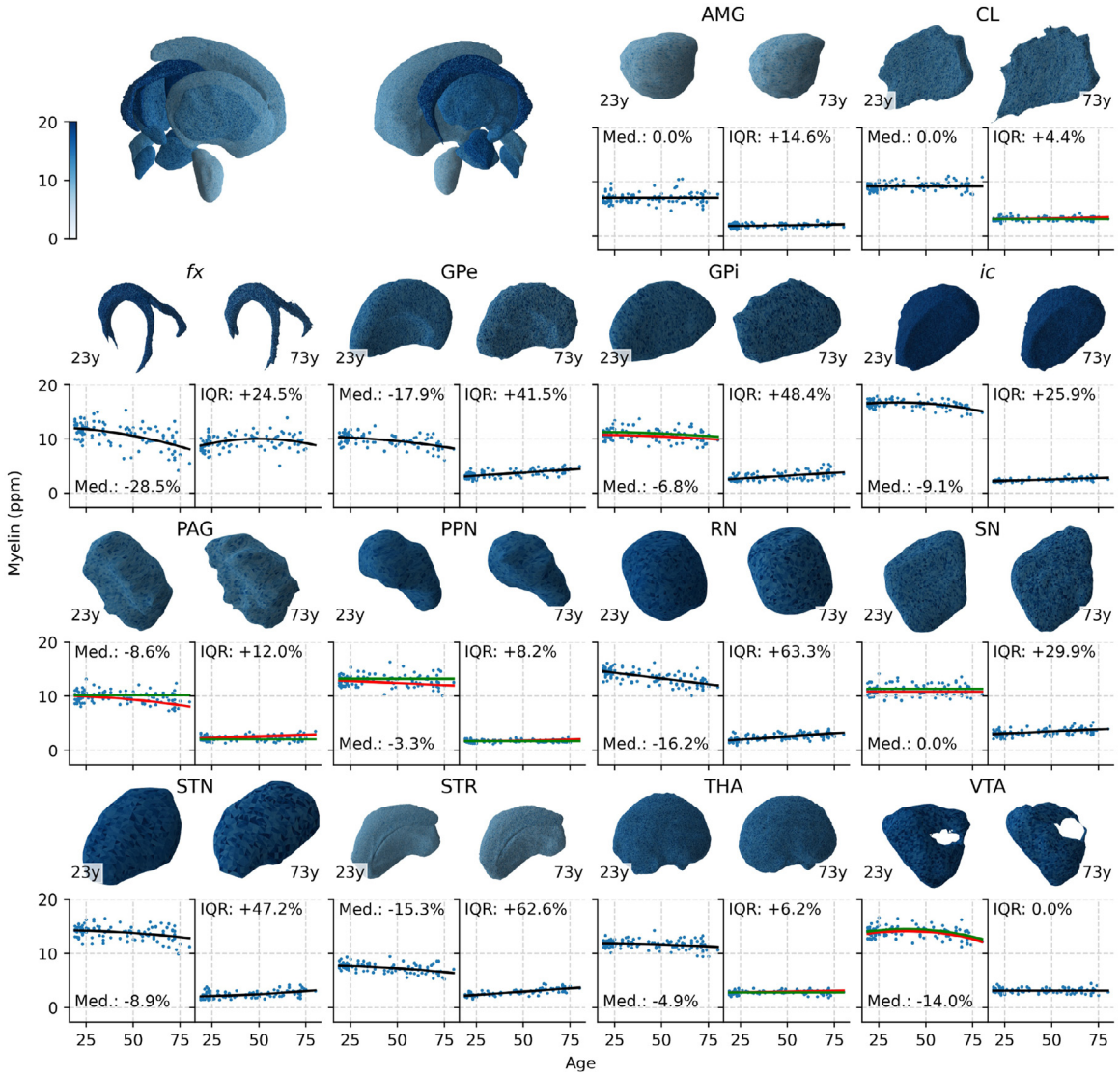


**Fig. 8.** Age-related changes in myelin content. The meshes are based on the young (18–30 years old, mean 23; left) and elderly (70–80 years old, mean 73; right) participants after a non-linear transformation to MNI2009b space. Mesh colors illustrate the model predictions for the median and IQR of myelin distributions at 23 (left) and 73 (right) years old, corresponding to the mean ages of the participant groups on which the meshes were based. Colors in the top-left meshes of all structures indicate model predictions at 23 years old. In case the winning model did not include sex as a predictor variable, the model predictions are shown in black lines; otherwise, green and orange lines are used for the predictions for women and men, respectively. The total amount of change in median (Med.) and IQR are shown in each scatterplot. The ventricles are assumed to have no myelin and are excluded from this graph. (For interpretation of the references to color in this figure legend, the reader is referred to the web version of this article.)

analyzing changes the median and IQR of thickness, which depend on the structure's shape. Specifically, when changes in the median thickness and volume point in the same direction (as is the case in, e.g., the lateral ventricles, striatum), this suggests overall thickening or thinning of a structure. Instead, increases in median thickness combined with decreases in volume can indicate atrophy in a thinner part of the structure, as this would decrease the amount of voxels with relatively low thickness, increasing the median thickness. This specific effect appeared to be present in the ventral tegmental area, pedunculopontine nucleus and periaqueductal gray. Furthermore, increases in IQR indicate decreases in structure regularity, which was observed in the globus pallidus interna, substantia nigra, periaqueductal gray, pedunculopontine nucleus, and red nucleus.

A third potential effect of atrophy is a change in the location of individual structures relative to the neurocranium (Keuken et al., 2017; 2013; Kitajima et al., 2008): As the brain atrophies, the resulting physical space is filled with CSF, leading to location shifts of other brain structures. For the majority of brain structures under investigation, we observed location shifts in the lateral and inferior direction (Fig. 10). The center of mass of the lateral and third ventricles and the claustrum also shifted in the posterior direction; the fornix and striatum shifted in anterior direction.

Combined, we observed age-related changes in all measures: iron, myelin, volume, thickness, and location. These effects were in line with the expected effects of iron accumulation, myelin degradation, and atrophy, but there appeared to be strong between-region variability in the degree to which regions change with age, which we focus on in the next section.

### 3.2. Between-structure variability in maturation

Because the winning models of age-related change trajectories included either linear or quadratic influences of age, the parameter estimates of the different models cannot be directly compared. To provide

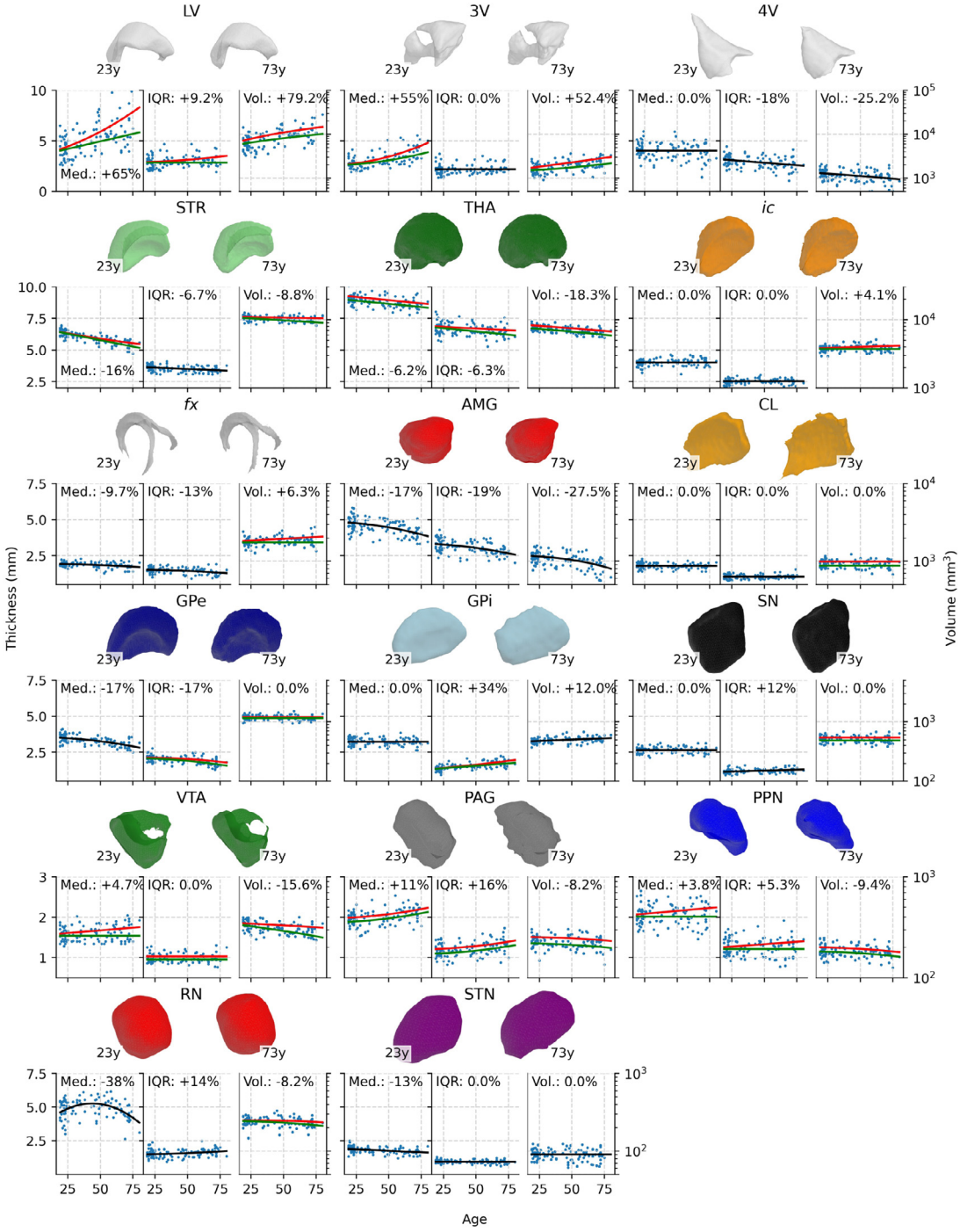


**Fig. 9.** Age-related changes in structure morphometry. The meshes are based on the young (18–30 years old, mean 23; left) and elderly (70–80 years old, mean 73; right) participants after a non-linear transformation to MNI2009b space. The lines in each scatterplot visualize the winning model predictions. In case the winning model did not include sex as a predictor variable, the model predictions are shown in black lines; otherwise, green and orange lines are used for the predictions for women and men, respectively. The total amount of change in median (Med.) and IQR of thickness and volume (Vol.) are shown in each scatterplot. (For interpretation of the references to color in this figure legend, the reader is referred to the web version of this article.)

a quantity that summarizes the amount of age-related change (irrespective of the underlying model specification), we calculated the sum of the absolute yearly changes between 19 and 75 years old, relative to the model's predicted value at 19 years old to take into account baseline differences (see Fig. 5).

For each structure, we then plotted the total age-related change per metric as a radar chart in Fig. 11, which defines a 'fingerprint' of aging per structure. Formal comparison of these fingerprints by means of a correlation matrix would require more than 7 metrics to achieve sufficient statistical power and assess significance. Here, we are restricted to qualitative comparisons. These fingerprints suggest strong interregion variability in aging patterns, also within groups of structures that could be grouped on anatomical grounds such as the basal ganglia. However, similarities can be found between various individual structures. For example, the red nucleus and striatum both show strong increases in the IQR of iron and myelin, combined with increases in median iron and

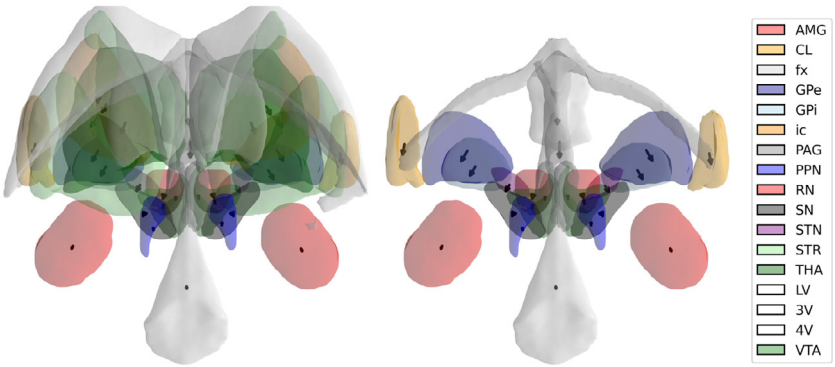


**Fig. 10.** Age-related changes in structure location, posterior view. Meshes were based on the young (18–30 years old) participants after non-linearly transforming to MNI2009b space. Arrows depict the model predictions for the location shift, starting at the center of mass of each structure in MNI2009b space, and pointing to the predicted center of mass of the structure at 75 years old. The left graph shows all 17 subcortical structures and ventricles under investigation, the right graph excludes the lateral ventricles, internal capsule, and thalamus, to improve the visibility of the smaller structures.

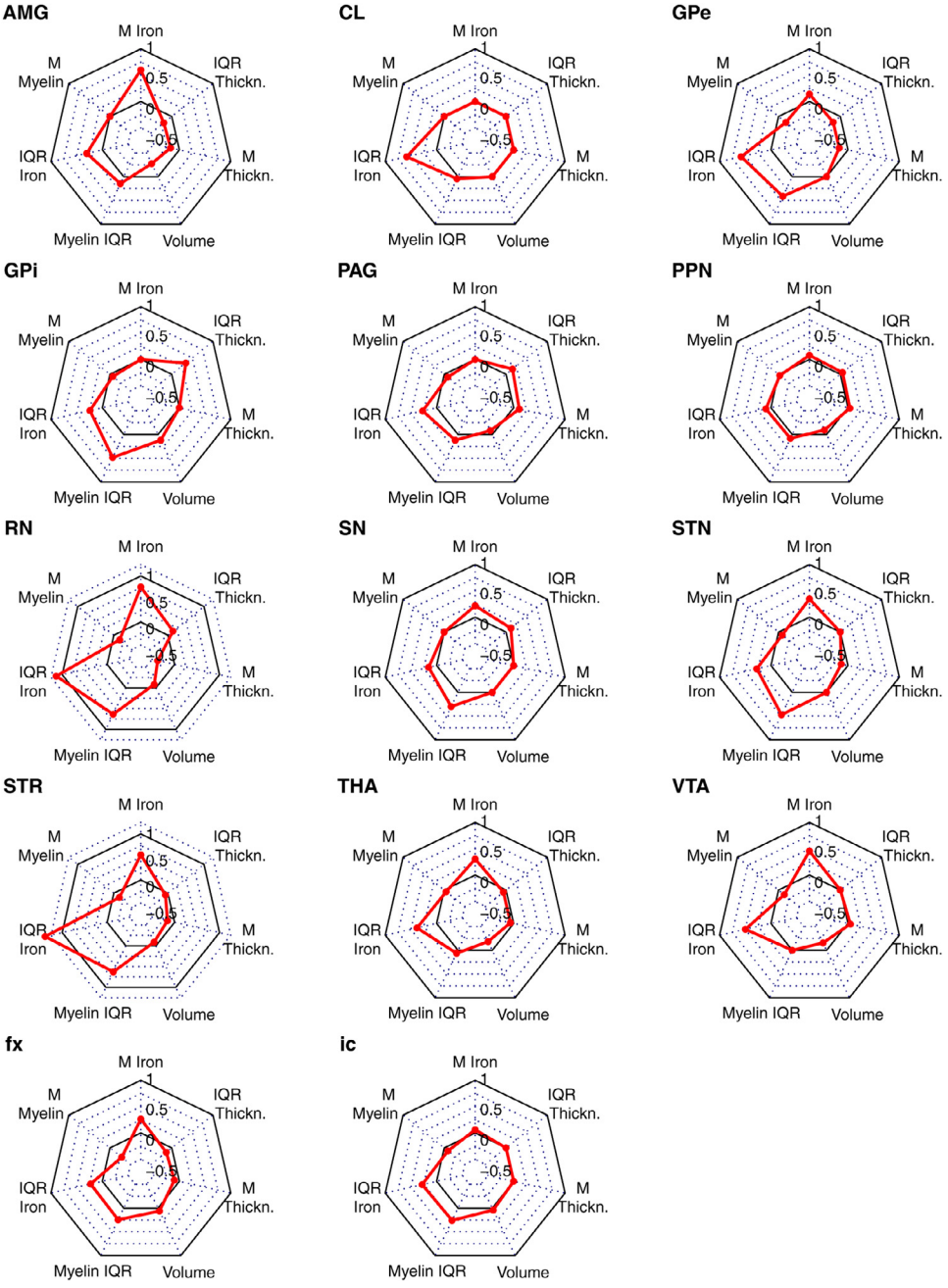


**Fig. 11.** Radar charts quantifying the total amount of age-related change (relative to the baseline value at 19 years old) along the seven metrics (radial axes), for each region separately. Each axis runs from −0.5 to 1, which correspond to total amounts of change equal to 50% in negative direction and 100% in positive direction, respectively. The axes for the red nucleus and striatum run to 1.25 to accommodate the large amounts of change in the IQR of iron in these regions. Solid lines indicate 0 (no change) and 1. Red dots indicate the measured amount of change. (For interpretation of the references to color in this figure legend, the reader is referred to the web version of this article.)

decreases in median myelin. Additionally, the aging patterns in the thalamus and ventral tegmental area suggest similarities, with median and IQR iron increases of comparable sizes, and relative stability on the other metrics. Median and IQR increases in iron combined with IQR increases in myelin were found in the substantia nigra and subthalamic nucleus, with the other measures remaining relatively stable. Finally, some structures including the periaqueductal gray, pedunculopontine nucleus, and internal capsule appear to remain relatively stable across all metrics.

## 4. Discussion

Interest in the human subcortex is rapidly growing in cognitive and clinical neuroscience due to the relevance of subcortical regions as (potential) targets for DBS and their role in cognition. Here, we studied 17 subcortical structures and ventricles in terms of their iron and myelin contents, their sizes, as well as the intricate age-related alterations. Our results highlight the heterogeneity in the subcortex, presenting the strong variability in iron, myelin, and morphometry that exists between structures. Furthermore, our results indicate global effects of iron accumulation, myelin degradation, and atrophy in the subcortex across the normal adult lifespan, and strong variability in the extent to which the different structures are affected by each type of age-related change.

To better navigate the rich landscape of subcortical aging, we also share our results in an online app (Fig. S4, https://subcortex.eu/app) that can be used to create interactive and intuitive 3D visualizations of the human subcortex across the lifespan and across modalities. It allows for inspection and reuse of the underlying models and data of each individual structure. The app was designed in a flexible way, so that it can be augmented with more structures and contrasts to expand it to a comprehensive chart of the human subcortex. The underlying data can readily be downloaded for further analyses.

Understanding the aging processes in the subcortex is paramount in research and in clinical practice. While iron accumulation and myelin degradation are part of normal aging processes, increased accumulation and myelin degradation are part of multiple neurodegenerative disorders including Parkinson's and Huntington's disease (Andersen et al., 2014; Collingwood and Davidson, 2014; Ward et al., 2014; Zecca et al., 2004). An accurate description of the distributions of iron and myelin across the lifespan in health provides a frame of reference against which pathological iron accumulation and myelin degradation can be contrasted, and can prove useful in the development of biomarkers for disease (Guan et al., 2017; Mancini et al., 2020; Martin et al., 2008; Schenck and Zimmerman, 2004; Zecca et al., 2004).

Iron and myelin are also the two main determinants of MRI contrast. Many subcortical structures, such as the subthalamic nucleus, cannot readily be distinguished on conventional T1-weighted MRI images due to a lack of contrast with nearby regions. Because of the limited visibility of subcortical structures on conventional MR images, a common practice is to use atlases to locate individual structures (Devlin and Poldrack, 2007; Evans et al., 2012). Stereotactic atlases based on *post mortem* tissue are often used for planning DBS surgery, and probabilistic MRI atlases are conventionally used in cognitive neuroscientific research. Subcortical MRI atlases are growing in numbers (Keuken et al., 2014; Lau et al., 2020; Pauli et al., 2018; Trutti et al., 2021; Ye et al., 2021) due to improvements in MRI resolution and contrasts. However, MRI atlases are typically developed using anatomical images obtained from young participants, which can cause biases when such atlases are subsequently used to infer anatomical information in older participants or patient populations (Evans et al., 2012; Keuken et al., 2013; Samanez-Larkin and D'Esposito, 2008). In cognitive neuroscience research, it is common to apply spatial normalization procedures to a group space to account for individual differences in anatomy, but consistent deviations from the group template are likely to introduce normalization errors (Samanez-Larkin and D'Esposito, 2008). These biases can result from iron accumulation and myelin degradation (which change the contrast of images) and from atrophy (which change the size and the location of structures). Our results can help understand the biases that could occur when conventional MRI atlases, based on young participants, are used to analyze data from older participants, and call for the development of age-specific MRI atlases of the subcortex to remedy these biases.

The between-region variation in iron contents has important consequences for blood oxygenation level dependent (BOLD) functional MRI. Because iron decreases $T2^*$ relaxation times, on which contrast-to-noise ratios (CNR) of BOLD-fMRI sequences depend, BOLD CNR varies substantially between regions. For instance, within young participants, the CNR in the red nucleus is expected to be 74% lower than in the amygdala, when using an echo time of 42 ms at 7 T (corresponding to the $T2^*$ of the amygdala in young participants), solely due to the differences in $T2^*$ (see supplement for details). Age-related alterations in iron contents can have similar effects. For instance, the CNR in the red nucleus at 50 years old is 32% lower than at 19 years old when using an echo time of 18 ms at 7 T (corresponding to the $T2^*$ of the red nucleus at 19 years old). Thus, iron deposition can confound fMRI studies into age-related changes of BOLD responses.

However, substantial gains in CNR can be achieved by optimizing the echo time to meet the specific requirements of studying a structure of interest (see also De Hollander et al., 2017; Miletić et al., 2020). For instance, when targeting the red nucleus, decreasing the echo time to 18 ms (corresponding to the $T2^*$ of the red nucleus at 19 years old) is expected to lead to a 62% higher CNR compared to an echo time of 42 ms (which would be optimal to target the amygdala). Similarly, the echo time can be adjusted to partially mitigate the effects of age-related changes in $T2^*$: By decreasing the echo time from 18 ms to 13 ms (corresponding to the $T2^*$ of the red nucleus at 50 years old), a modest 6% increase in CNR can be expected. Using our online app as a resource for participant-specific predictions of R1, $R2^*$, and QSM values, we envision the use of MRI protocols tailored to the structure of interest and the participant's age and sex.

### 4.1. Comparison with previous aging studies

The majority of previous subcortical aging studies focused on volume metrics. Direct comparison with other studies is hindered by differences in anatomical region definitions (e.g., striatum versus putamen and caudate, entire pallidum versus internal and external segments), delineation methods, modeling approaches (parametric versus non-parametric), and differences in age ranges (see also Coupé et al., 2017; Walhovd et al., 2016), although our results fall in line with previous reports.

The thalamus and striatum are studied most often and have consistently been reported to decrease in volume across the adult lifespan. Studies differ, however, in the shape of the reported trajectories: Some suggest quadratic or cubic volume decreases in both thalamus (Coupé et al., 2017; Dima et al., 2021; Potvin et al., 2016; Tullo et al., 2019; Wang et al., 2019) and striatum (Coupé et al., 2017; Potvin et al., 2016; Tullo et al., 2019), others show linearity or suggest approximate linearity (Fjell et al., 2013; Sullivan et al., 2004; Walhovd et al., 2011; Wang et al., 2019). In concordance with the latter reports, our data suggest linear volume decreases, although we cannot rule out that small non-linear trends are present that we could not detect with our sample size.

Other subcortical structures previously studied include the globus pallidus, for which linear and quadratic volume decreases have been reported (Coupé et al., 2017; Fjell et al., 2013; Goodro et al., 2012; Tullo et al., 2019; Walhovd et al., 2011; Wang et al., 2019), although not consistently: Other studies have reported stable volumes across age (Inano et al., 2013; Jernigan et al., 2001). Our data suggested a stable volume in the external part of the globus pallidus, but we found a volume increase in the internal part (c.f. Keuken et al., 2017, who found volume increases in the external part). In the amygdala, we found quadratic volume decreases. Recent large-sample studies (Coupé et al., 2017; Dima et al., 2021) suggest that the amygdala volume remains stable between approximately 20–70 years old, and then declines. This implies that the maturation pattern strongly depends on the age range

studied, which could explain the discrepancies in results from earlier studies that reported stable volumes (Jernigan et al., 2001), and linear (Narvacan et al., 2017; Walhovd et al., 2011; Wang et al., 2019) and quadratic (Goodro et al., 2012; Inano et al., 2013) volume decreases.

Volume increases in the lateral ventricles have been shown to be quadratic previously (Inano et al., 2013; Walhovd et al., 2005; Walhovd et al., 2011; see also Goodro et al., 2012). While our thickness estimates indeed suggest quadratic increases, the volume estimates instead indicate linear increases. Earlier reports on volume changes in the fourth ventricle are not consistent: Some studies have reported volume increases (Walhovd et al., 2005) or stable volumes in the fourth ventricle (Inano et al., 2013; Keuken et al., 2017; Walhovd et al., 2011). Here, we found a volume decrease in the fourth ventricle.

While our method of estimating iron contents has not been used to study aging before, our results can be compared to studies focusing on (q)MRI markers of iron. Daugherty and Raz (2013) provided a meta-analysis of early (q)MRI studies on iron accumulation in the caudate, red nucleus, and substantia nigra, and concluded that iron accumulates in these regions. The underlying studies used R2(*), the field-dependent increase in R2, and phase information based on susceptibility weighted imaging (SWI) as markers for iron. Later studies employing QSM and T2*/R2* are generally consistent with these findings (Acosta-Cabronero et al., 2016; Betts et al., 2016; Callaghan et al., 2014; Keuken et al., 2017; Li et al., 2021; Zhang et al., 2018; but see Khattar et al., 2021, who report no change in these areas). In line with these reports, our results suggest iron accumulation in these regions, specifically in inverted U-shaped trajectories.

Studies on iron accumulation in other subcortical regions have varying and sometimes conflicting conclusions. Daugherty and Raz (2013) also suggested iron accumulation in the globus pallidus. Our data found linear iron accumulation in the external, but no change in the internal segment. In contrast, Keuken et al. (2017) reported no change in T2* or QSM for the external segment (potentially indicating stable iron concentrations). They did report a T2* increase (which could indicate iron decreases) and stable QSM in the internal segment. Khattar et al. (2021) showed no change the SWI phase in the (entire) globus pallidus, in line with the findings from Li et al. (2021) who studied QSM as an iron marker. Our results suggest linear iron accumulation in the amygdala as well. Based on QSM, Acosta-Cabronero et al. (2016) instead reported stable iron contents in the amygdala (similar to Zhang et al. (2018), although the difference in age ranges under study hinders direct comparison). Finally, we also found inverted U-shaped iron trajectories in the thalamus. Khattar et al. (2021) found decreasing SWI phase in thalamus (suggesting iron increases), but Li et al. (2021) showed decreasing QSM values in the thalamus which instead suggests iron decreases.

Most earlier studies focusing on age-related change in myelin used the ratio of T1w/T2w as a myelin marker, which is controversial (Arshad et al., 2016; Glasser and van Essen, 2011; Grydeland et al., 2019; Uddin et al., 2018; 2019). Inverted U-shape trajectories of T1w/T2w have been reported in both cortex (Grydeland et al., 2019), and in the striatum and pallidum (Tullo et al., 2019). Our data instead suggest quadratic but monotonic decreases in myelination in these areas. Other microstructure markers include DTI-derived metrics such as fractional anisotropy and mean diffusivity, which suggested linear declines in microstructure of the thalamus, putamen, and caudate (Cherubini et al., 2009; Wang et al., 2010). Similarly, Callaghan et al. (2014) used magnetization transfer as a microstructure marker in the thalamus and caudate, which also suggested linear declines. Our results for the white matter tracts showed demyelination in fornix and the internal capsule, the pattern of which is qualitatively in line with earlier studies (Lebel et al., 2012; Madden et al., 2012) that analyzed DTI measures in white matter tracts.

More recently, myelin-water fraction (MWF; MacKay et al., 1994) estimation is gaining popularity as a proxy for myelin. Arshad et al. (2016) demonstrated that MWF in the internal capsule shows an inverted U-shaped age-related change trajectory, which shows qualitative similarity to our results in the internal capsule. Finally, Khattar et al. (2021) used MWF to analyze subcortical nuclei, which suggested inverted U-shaped aging trajectories across many subcortical regions, even for those where our results suggested stable myelin contents or monotonically decreasing trends.

### 4.2. Limitations

The present study has several limitations. A first limitation is the estimation of iron and myelin, which was done using simplified biophysical models that translate qMRI contrast values into the most likely underlying iron and myelin concentrations. The basic assumption underlying these models is that qMRI values are linearly related to iron and myelin concentrations. This is supported by previous studies (Mangeat et al., 2015; Marques et al., 2017; Metere and Möller, 2018; Rooney et al., 2007; Stüber et al., 2014).

Stüber et al. (2014) fit the parameters of their linear models using the iron, myelin concentrations and qMRI values in a single *post mortem* specimen, across many voxels. Metere and Möller (2018) generalized this approach by fitting the linear models on population-average myelin, iron concentrations and qMRI values, across many regions. The literature on the population-average iron and myelin concentrations, however, is sparse, especially in the case of myelin. This sparsity required us to estimate myelin contents of several subcortical regions using a *post mortem* specimen, which in turn required additional simplifying assumptions. The lack of a well-established, quantified 'ground truth' of myelin concentrations across the human brain is a limitation not only for the accuracy of the estimated calibration curve, but also prevents us from validating our results directly against it.

Our myelin estimates can be validated indirectly by qualitative comparison with observations from earlier reports that rely on other methods. While there is currently no exact qMRI marker of myelin, the aforementioned MWF estimation (MacKay et al., 1994) has been shown to be a relatively accurate method (Mancini et al., 2020). Khattar et al. (2021) reported MWF estimates in subcortical regions, and consistent with our results, their data suggest that myelin concentrations in subcortical gray matter regions may exceed myelin concentrations of cortical gray matter. Similarly, comparison with histology suggests that optical densities of myelin stains in deep gray matter regions such as the thalamus and globus pallidus are higher than cortical gray matter (e.g., Hametner et al., 2018).

Despite their limitations, our estimates of iron and myelin —compared to qMRI values— offers a distinct advantage in terms of interpretation. Multiple previous studies (reviewed above) into age-related changes aim to infer changes in iron concentrations by relying on a single (q)MRI metric such R2* or QSM, but R2* (Li et al., 2009) and QSM (e.g., Hametner et al., 2018; Liu et al., 2015) have been shown to also correlate with myelin concentrations (see also Daugherty and Raz, 2015). Similarly, there currently exists no perfect method to estimate myelin contents in vivo (Mancini et al., 2020), and while R1 covaries with myelin, studies suggest that it also covaries with iron (Ogg and Steen, 1998; Rooney et al., 2007; Stüber et al., 2014; but see Steen et al., 2000). As such, disentangling the contributions of iron and myelin to qMRI contrasts requires simultaneously consideration of multiple qMRI contrasts at once. Future studies that quantify iron and myelin concentrations across the brain, for example using systematic chemical assays or advanced microscopy (e.g. Brammerloh et al., 2021) on *post mortem* materials, can provide key information to validate and further improve upon our models. Finally, qMRI measurements are also prone to biases, for instance B1 inhomogeneities in R1 mapping (Haast et al., 2016), which are recalibrated when transforming qMRI values to myelin and iron estimates.

A second limitation is that the number of structures included in these studies is still limited. We intend to expand the number of structures in our future efforts. The hippocampus is of particular interest in the

context of aging due to its well-known atrophy associated with cognitive decline and neurodegenerative disease (Bettio et al., 2017). However, given its cortical origin, the hippo-campus has not been prioritized in this research and at present cannot be delineated by the MASSP algorithm. Since gold standard manual delineations have not been performed on the present data, we are currently unable to confirm the reliability of other algorithms for hippocampal delineation on our specific data. We intend to incorporate the hippocampus in MASSP in a future study.

Third, we cannot exclude age-related changes in parcellation accuracy. This is a general problem with aging studies, as parcellation accuracy tends to decrease with age due to decreased contrast between structures, even when structures are delineated manually. We relied on the MASSP algorithm (Bazin et al., 2020) to parcellate the 17 subcortical regions and ventricles in each participant individually. The performance of MASSP, like manual delineations, varies per structure, and depends on structure size and contrast (Alkemade et al., 2021). Compared to manual delineations, the performance of MASSP also tends to decrease with age. Fortunately, the impact of age-related biases in parcellation was shown to be limited for the quantitative MRI measures (Bazin et al., 2020) on which the iron and myelin estimates are based, suggesting that the age-related changes in myelin and iron are unlikely to be caused by age-related differences in parcellation performance. On the other hand, size estimates (volume and to a lesser extent thickness) are more susceptible to the age-related changes in parcellation quality. Here, we used an improved version of MASSP to mitigate these effects and could observe increased delineation accuracy for ventricles, fornix, claustrum, GPi and VTA (see Fig. S3). However, a replication of the age dependency study of Bazin et al. (2020) using the improved version of MASSP did not show much improvement in the consistency of thickness and volume estimate in smaller structures, where we cannot exclude age-related decreases in parcellation accuracy. While other automated parcellation algorithms incorporate certain structures of interest (such as the hippocampus, see above), we are not aware of any algorithm that can parcellate the same breadth of subcortical regions on qMRI data as MASSP. Future developments of MASSP or other algorithms might improve parcellation accuracy and thereby improve the robustness of models of age-related changes.

Finally, we are limited to descriptions of the age-related changes that result from iron accumulation, myelin degradation, and atrophy. While our results indicate a between-region heterogeneity in the age-related changes, they do not explain why certain regions appear to change more than others with increasing age. Similarly, we did not study the specific relation between qMRI metrics and morphometry (Lorio et al., 2016; Tardif et al., 2017; Weiskopf et al., 2015).

### 4.3. Conclusions

Our results extend previous studies into aging patterns of the subcortex, which focus on a smaller number of typically large subcortical areas, often based on MRI with lower field strengths (Aquino et al., 2009; Cherubini et al., 2009; Daugherty and Raz, 2013; 2016; Fjell et al., 2013; Greenberg et al., 2008; Herting et al., 2018; Keuken et al., 2017; Khattar et al., 2021; Li et al., 2014; Raz, 2004; Raz et al., 2005; Raz and Rodrigue, 2006; Raznahan et al., 2014; Walhovd et al., 2005; Wang et al., 2019). Experiments using very large numbers of participants detected complex nonlinear age-related changes in some subcortical structures (Coupé et al., 2017; Dima et al., 2021; Fjell et al., 2013). Our study had a more modest sample size, which did not allow to evaluate complex non-linear trends. On the other hand, by leveraging an open database of ultra-high field 7 T quantitative MRI, we could provide a first view on many structures and variables at once, which may be refined as more 7 T quantitative MRI data sets become available. As such, our study provides a richer and more extensible description of subcortical composition, morphometry and aging.

## Data and code availability statement

A prior version of the individual qMRI maps has been released as AHEAD (Alkemade et al., 2020a) can be found at https://doi.org/10.21942/uva.10007840.v1. All derived participant-wise and region-wise measures can be downloaded from our app at https://subcortex.eu/app. All code used to estimate the models and produce the figures can be found at https://osf.io/mvdbe/.

## Declaration of Competing Interest

Authors declare that they have no conflict of interest.

## Credit authorship contribution statement

**Steven Miletić:** Conceptualization, Methodology, Software, Validation, Formal analysis, Investigation, Data curation, Writing – original draft, Writing – review & editing, Visualization. **Pierre-Louis Bazin:** Conceptualization, Methodology, Investigation, Software, Supervision, Writing – original draft, Writing – review & editing, Formal analysis, Data curation. **Scott J.S. Isherwood:** Writing – review & editing. **Max C. Keuken:** Writing – review & editing. **Anneke Alkemade:** Conceptualization, Methodology, Validation, Investigation, Resources, Data curation, Writing – original draft, Writing – review & editing, Supervision, Project administration, Funding acquisition. **Birte U. Forstmann:** Conceptualization, Methodology, Validation, Investigation, Resources, Data curation, Supervision, Project administration, Funding acquisition.

## Acknowledgments

This research was financially supported by STW/NWO (#14017; BUF and AA), ERC PoC (BUF), NWO Vici (016.Vici.185.052; BUF), and Stichting Ammodo (2019; BUF).

## Supplementary material

Supplementary material associated with this article can be found, in the online version, at 10.1016/j.neuroimage.2022.118872

## References

Acosta-Cabronero, J., Betts, M.J., Cardenas-Blanco, A., Yang, S., Nestor, P.J., et al., 2016. In vivo MRI mapping of brain iron deposition across the adult lifespan. J. Neurosci. 36 (2), 364–374. doi:10.1523/JNEUROSCI.1907-15.2016.

Akaike, H., 1973. Information theory and an extension of the maximum likelihood principle. In: Petrov, B.N., Caski, F. (Eds.), Proceedings of the Second International Symposium on Information Theory. Akademiai Kiado, Budapest, pp. 267–281.

Alkemade, A., Keuken, M.C., Forstmann, B.U., 2013. A perspective on terra incognita: uncovering the neuroanatomy of the human subcortex. Front. Neuroanat. 7 (2), 267–277. doi:10.3389/fnana.2013.00040.

Alkemade, A., Mulder, M.J., Groot, J.M., Isaacs, B.R., van Berendonk, N., Lute, N., Isherwood, S.J.S., Bazin, P.-L., Forstmann, B.U., et al., 2020. The Amsterdam ultra-high field adult lifespan database (AHEAD): a freely available multimodal 7 Tesla submillimeter magnetic resonance imaging database. NeuroImage 221, 117200. doi:10.1016/j.neuroimage.2020.117200.

Alkemade, A., Mulder, M.J., Trutti, A.C., Forstmann, B.U., et al., 2021. Manual delineation approaches for direct imaging of the subcortex. Brain Struct. Funct. doi:10.1007/s00429-021-02400-x.

Alkemade, A., Pine, K., Kirilina, E., Keuken, M.C., Mulder, M.J., Balesar, R., Groot, J.M., Bleys, R.L.A.W., Trampel, R., Weiskopf, N., Herrler, A., Möller, H.E., Bazin, P.-l., Forstmann, B.U., et al., 2020. 7 Tesla MRI followed by histological 3D reconstructions in whole-brain specimens. Front. Neuroanat. 14 (October), 1–11. doi:10.3389/fnana.2020.536838.

Andersen, H.H., Johnsen, K.B., Moos, T., 2014. Iron deposits in the chronically inflamed central nervous system and contributes to neurodegeneration. Cell. Mol. Life Sci. 71 (9), 1607–1622. doi:10.1007/s00018-013-1509-8.

Aquino, D., Bizzi, A., Grisoli, M., Garavaglia, B., Bruzzone, M.G., Nardocci, N., Savoiardo, M., Chiapparini, L., et al., 2009. Age-related iron deposition in the basal ganglia: quantitative analysis in healthy subjects. Radiology 252 (1), 165–172.

Arshad, M., Stanley, J.A., Raz, N., 2016. Adult age differences in subcortical myelin content are consistent with protracted myelination and unrelated to diffusion tensor imaging indices. NeuroImage 143, 26–39. doi:10.1016/j.neuroimage.2016.08.047.

Avants, B., Epstein, C., Grossman, M., Gee, J., 2008. Symmetric diffeomorphic image registration with cross-correlation: evaluating automated labeling of elderly and neurodegenerative brain. Med. Image Anal. 12 (1), 26–41. doi:10.1016/j.media.2007.06.004.

Bazin, P.-L., Alkemade, A., Mulder, M.J., Henry, A.G., Forstmann, B.U., et al., 2020. Multi-contrast anatomical subcortical structures parcellation. eLife 9, 1–23. doi:10.7554/eLife.59430.

Bazin, P.-L., Alkemade, A., van der Zwaag, W., Caan, M., Mulder, M.J., Forstmann, B.U., et al., 2019. Denoising high-field multi-dimensional MRI with local complex PCA. Front. Neurosci. 13 (October), 1–10. doi:10.3389/fnins.2019.01066.

Bazin, P.-L., Weiss, M., Dinse, J., Schäfer, A., Trampel, R., Turner, R., et al., 2014. A computational framework for ultra-high resolution cortical segmentation at 7 Tesla. NeuroImage 93, 201–209. doi:10.1016/j.neuroimage.2013.03.077.

Bettio, L.E.B., Rajendran, L., Gil-Mohapel, J., 2017. The effects of aging in the hippocampus and cognitive decline. Neurosci. Biobehav. Rev. 79 (March), 66–86. doi:10.1016/j.neubiorev.2017.04.030.

Betts, M.J., Acosta-Cabronero, J., Cardenas-Blanco, A., Nestor, P.J., Düzel, E., 2016. High-resolution characterisation of the aging brain using simultaneous quantitative susceptibility mapping (QSM) and R2* measurements at 7 T. NeuroImage 138, 43–63. doi:10.1016/j.neuroimage.2016.05.024.

Birkl, C., Langkammer, C., Golob-Schwarzl, N., Leoni, M., Haybaeck, J., Goessler, W., Fazekas, F., Ropele, S., et al., 2016. Effects of formalin fixation and temperature on MR relaxation times in the human brain. NMR Biomed. 29 (4), 458–465. doi:10.1002/nbm.3477.

Brammerloh, M., Morawski, M., Friedrich, I., Reinert, T., Lange, C., Pelicon, P., Vavpetič, P., Jankuhn, S., Jäger, C., Alkemade, A., Balesar, R., Pine, K., Gavriilidis, F., Trampel, R., Reimer, E., Arendt, T., Weiskopf, N., Kirilina, E., et al., 2021. Measuring the iron content of dopaminergic neurons in substantia nigra with MRI relaxometry. NeuroImage 239 (June). doi:10.1016/j.neuroimage.2021.118255.

Caan, M.W.A., Bazin, P.-L., Marques, J.P., Hollander, G., Dumoulin, S.O., Zwaag, W., et al., 2019. MP2RAGEME: T1, T2*, and QSM mapping in one sequence at 7 Tesla. Hum. Brain Mapp. 40 (6), 1786–1798. doi:10.1002/hbm.24490.

Callaghan, M.F., Freund, P., Draganski, B., Anderson, E., Cappelletti, M., Chowdhury, R., Diedrichsen, J., FitzGerald, T.H.B., Smittenaar, P., Helms, G., Lutti, A., Weiskopf, N., et al., 2014. Widespread age-related differences in the human brain microstructure revealed by quantitative magnetic resonance imaging. Neurobiol. Aging 35 (8), 1862–1872. doi:10.1016/j.neurobiolaging.2014.02.008.

Cherubini, A., Péran, P., Caltagirone, C., Sabatini, U., Spalletta, G., et al., 2009. Aging of subcortical nuclei: microstructural, mineralization and atrophy modifications measured in vivo using MRI. NeuroImage 48 (1), 29–36. doi:10.1016/j.neuroimage.2009.06.035.

Collingwood, J.F., Davidson, M.R., 2014. The role of iron in neurodegenerative disorders: insights and opportunities with synchrotron light. Front. Pharmacol. 5 (August), 1–19. doi:10.3389/fphar.2014.00191.

Coupé, P., Catheline, G., Lanuza, E., Manjón, J.V., et al., 2017. Towards a unified analysis of brain maturation and aging across the entire lifespan: a MRI analysis. Hum. Brain Mapp. 38 (11), 5501–5518. doi:10.1002/hbm.23743.

Courchesne, E., Chisum, H.J., Townsend, J., Cowles, A., Covington, J., Egaas, B., Harwood, M., Hinds, S., Press, G.A., et al., 2000. Normal brain development and aging: quantitative analysis at in vivo MR imaging in healthy volunteers. Radiology 216 (3), 672–682. doi:10.1148/radiology.216.3.r00au37672.

Daugherty, A.M., Raz, N., 2013. Age-related differences in iron content of subcortical nuclei observed in vivo: a meta-analysis. NeuroImage 70, 113–121. doi:10.1016/j.neuroimage.2012.12.040.

Daugherty, A.M., Raz, N., 2015. Appraising the role of iron in brain aging and cognition: promises and limitations of MRI methods. Neuropsychol. Rev. 25 (3), 272–287. doi:10.1007/s11065-015-9292-y.

Daugherty, A.M., Raz, N., 2016. Accumulation of iron in the putamen predicts its shrinkage in healthy older adults: a multi-occasion longitudinal study. NeuroImage 128, 11–20. doi:10.1016/j.neuroimage.2015.12.045.

De Hollander, G., Keuken, M.C., van der Zwaag, W., Forstmann, B.U., Trampel, R., et al., 2017. Comparing functional MRI protocols for small, iron-rich basal ganglia nuclei such as the subthalamic nucleus at 7 T and 3 T. Hum. Brain Mapp. 38 (6), 3226–3248. doi:10.1002/hbm.23586.

Devlin, J.T., Poldrack, R.A., 2007. In praise of tedious anatomy. NeuroImage 37 (4), 1033–1041. doi:10.1016/j.neuroimage.2006.09.055.

Dima, D., Modabbernia, A., Papachristou, E., Doucet, G.E., Agartz, I., Aghajani, M., Akudjedu, T.N., Albajes-Eizagirre, A., Alnæs, D., Alpert, K.I., Andersson, M., Andreasen, N.C., Andreassen, O.A., Asherson, P., Banaschewski, T., Bargallo, N., Baumeister, S., Baur-Streubel, R., Bertolino, A., Bonvino, A., Boomsma, D.I., Borgwardt, S., Bourque, J., Brandeis, D., Breier, A., Brodaty, H., Brouwer, R.M., Buitelaar, J.K., Busatto, G.F., Buckner, R.L., Calhoun, V., Canales-Rodríguez, E.J., Cannon, D.M., Caseras, X., Castellanos, F.X., Cervenka, S., Chaim-Avancini, T.M., Ching, C.R.K., Chubar, V., Clark, V.P., Conrod, P., Conzelmann, A., Crespo-Facorro, B., Crivello, F., Crone, E.A., Dale, A.M., Davey, C., de Geus, E.J.C., de Haan, L., de Zubicaray, G.I., den Braber, A., Dickie, E.W., Di Giorgio, A., Doan, N.T., Dørum, E.S., Ehrlich, S., Erk, S., Espeseth, T., Fatouros-Bergman, H., Fisher, S.E., Fouche, J.P., Franke, B., Frodl, T., Fuentes-Claramonte, P., Glahn, D.C., Gotlib, I.H., Grabe, H.J., Grimm, O., Groenewold, N.A., Grotegerd, D., Gruber, O., Gruner, P., Gur, R.E., Gur, R.C., Harrison, B.J., Hartman, C.A., Hatton, S.N., Heinz, A., Heslenfeld, D.J., Hibar, D.P., Hickie, I.B., Ho, B.C., Hoekstra, P.J., Hohmann, S., Holmes, A.J., Hoogman, M., Hosten, N., Howells, F.M., Hulshoff Pol, H.E., Huyser, C., Jahanshad, N., James, A., Jernigan, T.L., Jiang, J., Jönsson, E.G., Joska, J.A., Kahn, R., Kalnin, A., Kanai, R., Klein, M., Klyushnik, T.P., Koenders, L., Koops, S., Krämer, B., Kuntsi, J., Lagopoulos, J., Lázaro, L., Lebedeva, I., Lee, W.H., Lesch, K.P., Lochner, C., Machielsen, M.W.J., Maingault, S., Martin, N.G., Martínez-Zalacaín, I., Mataix-Cols, D., Mazoyer, B., McDonald, C., McDonald, B.C., McIntosh, A.M., McMahon, K.L., McPhilemy, G., Menchón, J.M., Medland, S.E., Meyer-Lindenberg, A., Naaijen, J., Najt, P., Nakao, T., Nordvik, J.E., Nyberg, L., Oosterlaan, J., de la Foz, V.O.G., Paloyelis, Y., Pauli, P., Pergola, G., Pomarol-Clotet, E., Portella, M.J., Potkin, S.G., Radua, J., Reif, A., Rinker, D.A., Roffman, J.L., Rosa, P.G.P., Sacchet, M.D., Sachdev, P.S., Salvador, R., Sánchez-Juan, P., Sarró, S., Satterthwaite, T.D., Saykin, A.J., Serpa, M.H., Schmaal, L., Schnell, K., Schumann, G., Sim, K., Smoller, J.W., Sommer, I., Soriano-Mas, C., Stein, D.J., Strike, L.T., Swagerman, S.C., Tamnes, C.K., Temmingh, H.S., Thomopoulos, S.I., Tomyshev, A.S., Tordesillas-Gutiérrez, D., Trollor, J.N., Turner, J.A., Uhlmann, A., van den Heuvel, O.A., van den Meer, D., van der Wee, N.J.A., van Haren, N.E.M., van't Ent, D., van Erp, T.G.M., Veer, I.M., Veltman, D.J., Voineskos, A., Völzke, H., Walter, H., Walton, E., Wang, L., Wang, Y., Wassink, T.H., Weber, B., Wen, W., West, J.D., Westlye, L.T., Whalley, H., Wierenga, L.M., Williams, S.C.R., Wittfeld, K., Wolf, D.H., Worker, A., Wright, M.J., Yang, K., Yoncheva, Y., Zanetti, M.V., Ziegler, G.C., Thompson, P.M., Frangou, S., et al., 2021. Subcortical volumes across the lifespan: data from 18,605 healthy individuals aged 3–90 years. Hum. Brain Mapp. (December 2020) 1–18. doi:10.1002/hbm.25320.

Ding, L., Gold, J.I., 2013. The basal ganglia's contributions to perceptual decision making. Neuron 79 (4), 640–649. doi:10.1016/j.neuron.2013.07.042.

Ehrenberg, A.J., Nguy, A.K., Theofilas, P., Dunlop, S., Suemoto, C.K., Di Lorenzo Alho, A.T., Leite, R.P., Diehl Rodriguez, R., Mejia, M.B., Rüb, U., Farfel, J.M., de Lucena Ferretti-Rebustini, R.E., Nascimento, C.F., Nitrini, R., Pasquallucci, C.A., Jacob-Filho, W., Miller, B., Seeley, W.W., Heinsen, H., Grinberg, L.T., et al., 2017. Quantifying the accretion of hyperphosphorylated tau in the locus coeruleus and dorsal raphe nucleus: the pathological building blocks of early Alzheimer's disease. Neuropathol. Appl. Neurobiol. 43 (5), 393–408. doi:10.1111/nan.12387.

Evans, A.C., Janke, A.L., Collins, D.L., Baillet, S., et al., 2012. Brain templates and atlases. NeuroImage 62 (2), 911–922. doi:10.1016/j.neuroimage.2012.01.024.

Fasano, A., Lozano, A.M., 2015. Deep brain stimulation for movement disorders. Curr. Opin. Neurol. 28 (4), 423–436. doi:10.1097/WCO.0000000000000226.

Fields, R.D., 2015. A new mechanism of nervous system plasticity: activity-dependent myelination. Nat. Rev. Neurosci. 16 (12), 756–767. doi:10.1038/nrn4023.

Fjell, A.M., Westlye, L.T., Grydeland, H., Amlien, I., Espeseth, T., Reinvang, I., Raz, N., Holland, D., Dale, A.M., Walhovd, K.B., et al., 2013. Critical ages in the life course of the adult brain: nonlinear subcortical aging. Neurobiol. Aging 34 (10), 2239–2247. doi:10.1016/j.neurobiolaging.2013.04.006.

Forstmann, B.U., De Hollander, G., Van Maanen, L., Alkemade, A., Keuken, M.C., et al., 2017. Towards a mechanistic understanding of the human subcortex. Nat. Rev. Neurosci. 18, 57–65.

German, D.C., White, C.L., Sparkman, D.R., 1987. Alzheimer's disease: neurofibrillary tangles in nuclei that project to the cerebral cortex. Neuroscience 21 (2), 305–312. doi:10.1016/0306-4522(87)90123-0.

Glasser, M.F., van Essen, D.C., 2011. Mapping human cortical areas in vivo based on myelin content as revealed by T1- and T2-weighted MRI. J. Neurosci. 31 (32), 11597–11616. doi:10.1523/JNEUROSCI.2180-11.2011.

Good, C.D., Johnsrude, I.S., Ashburner, J., Henson, R.N.A., Friston, K.J., Frackowiak, R.S.J., et al., 2001. A voxel-based morphometric study of ageing in 465 normal adult human brains. NeuroImage 14 (1I), 21–36. doi:10.1006/nimg.2001.0786.

Goodro, M., Sameti, M., Patenaude, B., Fein, G., et al., 2012. Age effect on subcortical structures in healthy adults. Psychiatry Res. 203 (1), 38–45. doi:10.1016/j.pscychresns.2011.09.014.

Greenberg, D.L., Messer, D.F., Payne, M.E., MacFall, J.R., Provenzale, J.M., Steffens, D.C., Krishnan, R.R., et al., 2008. Aging, gender, and the elderly adult brain: an examination of analytical strategies. Neurobiol. Aging 29 (2), 290–302. doi:10.1016/j.neurobiolaging.2006.09.016.

Grydeland, H., Vértes, P.E., Váša, F., Romero-Garcia, R., Whitaker, K., Alexander-Bloch, A.F., Bjørnerud, A., Patel, A.X., Sederevičius, D., Tamnes, C.K., Westlye, L.T., White, S.R., Walhovd, K.B., Fjell, A.M., Bullmore, E.T., et al., 2019. Waves of maturation and senescence in micro-structural MRI markers of human cortical myelination over the lifespan. Cereb. Cortex 29 (3), 1369–1381. doi:10.1093/cercor/bhy330.

Guan, X., Xu, X., Zhang, M., 2017. Region-specific iron measured by MRI as a biomarker for Parkinson's disease. Neurosci. Bull. 33 (5), 561–567. doi:10.1007/s12264-017-0138-x.

Haacke, E.M., Cheng, N.Y.C., House, M.J., Liu, Q., Neelavalli, J., Ogg, R.J., Khan, A., Ayaz, M., Kirsch, W., Obenaus, A., et al., 2005. Imaging iron stores in the brain using magnetic resonance imaging. Magn. Reson. Imaging 23 (1), 1–25. doi:10.1016/j.mri.2004.10.001.

Haast, R.A.M., Ivanov, D., Formisano, E., Uludağ, K., et al., 2016. Reproducibility and reliability of quantitative and weighted T1 and T2* mapping for myelin-based cortical parcellation at 7 Tesla. Front. Neuroanat. 10 (NOV), 1–17. doi:10.3389/fnana.2016.00112.

Hahn, G.J., 1977. The hazards of extrapolation in regression analysis. J. Qual. Technol. 9 (4), 159–165. doi:10.1080/00224065.1977.11980791.

Hallgren, B., Sourander, P., 1958. The effect of age on the non-delHhaemin iron in the human brain. J. Neurochem. 3 (1), 41–51. doi:10.1111/j.1471-4159.1958.tb12607.x.

Hametner, S., Endmayr, V., Deistung, A., Palmrich, P., Prihoda, M., Haimburger, E., Menard, C., Feng, X., Haider, T., Leisser, M., Köck, U., Kaider, A., Höftberger, R., Robinson, S., Reichenbach, J.R., Lassmann, H., Traxler, H., Trattnig, S., Grabner, G., 2018. The influence of brain iron and myelin on magnetic susceptibility and effective transverse relaxation—A biochemical and histological validation study. NeuroImage 179 (May), 117–133. doi:10.1016/j.neuroimage.2018.06.007.

Herting, M.M., Johnson, C., Mills, K.L., Vijayakumar, N., Dennison, M., Liu, C., Goddings, A.L., Dahl, R.E., Sowell, E.R., Whittle, S., Allen, N.B., Tamnes, C.K., et al., 2018. Development of subcortical volumes across adolescence in males and females: a multisample study of longitudinal changes. NeuroImage 172 (January), 194–205. doi:10.1016/j.neuroimage.2018.01.020.

Hill, R.A., Li, A.M., Grutzendler, J., 2018. Lifelong cortical myelin plasticity and age-related degeneration in the live mammalian brain. Nat. Neurosci. 21 (5), 683–695. doi:10.1038/s41593-018-0120-6.

Hirsch, E.C., Graybiel, A.M., Agid, Y., 1988. Melanized dopaminergic neurons are differentially affected in Parkinson's disease. Nature 334, 345–348..

Ho, T.C., Gutman, B., Pozzi, E., Grabe, H.J., Hosten, N., Wittfeld, K., Völzke, H., Baune, B., Dannlowski, U., Förster, K., Grotegerd, D., Redlich, R., Jansen, A., Kircher, T., Krug, A., Meinert, S., Nenadic, I., Opel, N., Dinga, R., Veltman, D.J., Schnell, K., Veer, I., Walter, H., Gotlib, I.H., Sacchet, M.D., Aleman, A., Groenewold, N.A., Stein, D.J., Li, M., Walter, M., Ching, C.R.K., Jahanshad, N., Ragothaman, A., Isaev, D., Zavaliangos-Petropulu, A., Thompson, P.M., Sämann, P.G., Schmaal, L., et al., 2020. Subcortical shape alterations in major depressive disorder: findings from the ENIGMA major depressive disorder working group. Hum. Brain Mapp. (December 2019) 1–11. doi:10.1002/hbm.24988.

Inano, S., Takao, H., Hayashi, N., Yoshioka, N., Mori, H., Kunimatsu, A., Abe, O., Ohtomo, K., et al., 2013. Effects of age and gender on neuroanatomical volumes. J. Magn. Reson. Imaging 37 (5), 1072–1076. doi:10.1002/jmri.23910.

Jernigan, T.L., Archibald, S.L., Fennema-Notestine, C., Gamst, A.C., Stout, J.C., Bonner, J., Hesselink, J.R., et al., 2001. Effects of age on tissues and regions of the cerebrum and cerebellum. Neurobiol. Aging 22 (4), 581–594. doi:10.1016/S0197-4580(01)00217-2.

Keuken, M.C., Bazin, P.-L., Backhouse, K., Beekhuizen, S., Himmer, L., Kandola, A., Lafeber, J.J., Prochazkova, L., Trutti, A., Schäfer, A., Turner, R., Forstmann, B.U., et al., 2017. Effects of aging on T1, T2*, and QSM MRI values in the subcortex. Brain Struct. Funct. 222 (6), 2487–2505. doi:10.1007/s00429-016-1352-4.

Keuken, M.C., Bazin, P.L., Schäfer, A., Neumann, J., Turner, R., Forstmann, B.U., et al., 2013. Ultra-high 7T MRI of structural age-related changes of the subthalamic nucleus. J. Neurosci. 33 (11), 4896–4900. doi:10.1523/JNEUROSCI.3241-12.2013.

Keuken, M.C., Isaacs, B.R., Trampel, R., van der Zwaag, W., Forstmann, B.U., et al., 2018. Visualizing the human subcortex using ultra-high field magnetic resonance imaging. Brain Topogr. 31 (4), 513–545. doi:10.1007/s10548-018-0638-7.

Keuken, M.C., Müller-Axt, C., Langner, R., Eickhoff, S.B., Forstmann, B.U., Neumann, J., et al., 2014. Brain networks of perceptual decision-making: an fMRI ALE meta-analysis. Front. Hum. Neurosci. 8. doi:10.3389/fnhum.2014.00445.

Khattar, N., Triebswetter, C., Kiely, M., Ferrucci, L., Resnick, S.M., Spencer, R.G., Bouhrara, M., et al., 2021. Investigation of the association between cerebral iron content and myelin content in normative aging using quantitative magnetic resonance neuroimaging. NeuroImage 239 (June), 118267. doi:10.1016/j.neuroimage.2021.118267.

Kitajima, M., Korogi, Y., Kakeda, S., Moriya, J., Ohnari, N., Sato, T., Hayashida, Y., Hirai, T., Okuda, T., Yamashita, Y., et al., 2008. Human subthalamic nucleus: evaluation with high-resolution MR imaging at 3.0 T. Neuroradiology 50 (8), 675–681. doi:10.1007/s00234-008-0388-4.

Langkammer, C., Bredies, K., Poser, B.A., Barth, M., Reishofer, G., Fan, A.P., Bilgic, B., Fazekas, F., Mainero, C., Ropele, S., et al., 2015. Fast quantitative susceptibility mapping using 3D EPI and total generalized variation. NeuroImage 111, 622–630. doi:10.1016/j.neuroimage.2015.02.041.

Langkammer, C., Schweser, F., Krebs, N., Deistung, A., Goessler, W., Scheurer, E., Sommer, K., Reishofer, G., Yen, K., Fazekas, F., Ropele, S., Reichenbach, J.R., et al., 2012. Quantitative susceptibility mapping (QSM) as a means to measure brain iron? A post mortem validation study. NeuroImage 62 (3), 1593–1599. doi:10.1016/j.neuroimage.2012.05.049.

Lau, J.C., Xiao, Y., Haast, R.A.M., Gilmore, G., Uluday, K., MacDougall, K.W., Menon, R.S., Parrent, A.G., Peters, T.M., Khan, A.R., et al., 2020. Direct visualization and characterization of the human zona incerta and surrounding structures. Hum. Brain Mapp. 41 (16), 4500–4517. doi:10.1002/hbm.25137.

Lebel, C., Gee, M., Camicioli, R., Wieler, M., Martin, W., Beaulieu, C., et al., 2012. Diffusion tensor imaging of white matter tract evolution over the lifespan. NeuroImage 60 (1), 340–352. doi:10.1016/j.neuroimage.2011.11.094.

Lemaitre, H., Goldman, A.L., Sambataro, F., Verchinski, B.A., Meyer-Lindenberg, A., Weinberger, D.R., Mattay, V.S., et al., 2012. Normal age-related brain morphometric changes: nonuniformity across cortical thickness, surface area and gray matter volume? Neurobiol. Aging 33 (3), 617.e1–617.e9. doi:10.1016/j.neurobiolaging.2010.07.013.

LeVine, S.M., Wulser, M.J., Lynch, S.G., 1998. Iron quantification in cerebrospinal fluid. Anal. Biochem. 265 (1), 74–78. doi:10.1006/abio.1998.2903.

Li, W., van Tol, M.J., Li, M., Miao, W., Jiao, Y., Heinze, H.J., Bogerts, B., He, H., Walter, M., et al., 2014. Regional specificity of sex effects on subcortical volumes across the lifespan in healthy aging. Hum. Brain Mapp. 35 (1), 238–247. doi:10.1002/hbm.22168.

Li, Y., Sethi, S.K., Zhang, C., Miao, Y., Yerramsetty, K.K., Palutla, V.K., Gharabaghi, S., Wang, C., He, N., Cheng, J., Yan, F., Haacke, E.M., et al., 2021. Iron content in deep gray matter as a function of age using quantitative susceptibility mapping: a multicenter study. Front. Neurosci. 14 (January), 1–13. doi:10.3389/fnins.2020.607705.

Li, Z., Chen-Roetling, J., Regan, R.F., 2009. Increasing expression of H- or L-ferritin protects cortical astrocytes from hemin toxicity. Free Radic. Res. 43 (6), 613–621. doi:10.1080/10715760902942808.

Limousin, P., Pollak, P., Benazzouz, A., Hoffmann, D., Le Bas, J.-F., Perret, J.E., Benabid, A.-L., Broussolle, E., 1995. Effect on Parkinsonian signs and symptoms of bilateral subthalamic nucleus stimulation. Lancet 345 (8942), 91–95. doi:10.1016/S0140-6736(95)90062-4.

Liu, C., Li, W., Tong, K.A., Yeom, K.W., Kuzminski, S., et al., 2015. Susceptibility-weighted imaging and quantitative susceptibility mapping in the brain. J. Magn. Reson. Imaging 42 (1), 23–41. doi:10.1002/jmri.24768.

Lorio, S., Kherif, F., Ruef, A., Melie-Garcia, L., Frackowiak, R., Ashburner, J., Helms, G., Lutti, A., Draganski, B., et al., 2016. Neurobiological origin of spurious brain morphological changes: a quantitative MRI study. Hum. Brain Mapp. 37 (5), 1801–1815. doi:10.1002/hbm.23137.

Lozano, A.M., Lipsman, N., Bergman, H., Brown, P., Chabardes, S., Chang, J.W., Matthews, K., McIntyre, C.C., Schlaepfer, T.E., Schulder, M., Temel, Y., Volkmann, J., Krauss, J.K., et al., 2019. Deep brain stimulation: current challenges and future directions. Nat. Rev. Neurol. 15 (3), 148–160. doi:10.1038/s41582-018-0128-2.

MacKay, A., Whittall, K., Adler, J., Li, D., Paty, D., Graeb, D., et al., 1994. In vivo visualization of myelin water in brain by magnetic resonance. Magn. Reson. Med. 31 (6), 673–677. doi:10.1002/mrm.1910310614.

Madden, D.J., Bennett, I.J., Burzynska, A., Potter, G.G., kuei Chen, N., Song, A.W., et al., 2012. Diffusion tensor imaging of cerebral white matter integrity in cognitive aging. Biochim. Biophys. Acta 1822 (3), 386–400. doi:10.1016/j.bbadis.2011.08.003.

Mancini, M., Karakuzu, A., Cohen-Adad, J., Cercignani, M., Nichols, T.E., Stikov, N., et al., 2020. An interactive meta-analysis of MRI biomarkers of Myelin. eLife 9, 1–23. doi:10.7554/eLife.61523.

Mangeat, G., Govindarajan, S.T., Mainero, C., Cohen-Adad, J., 2015. Multivariate combination of magnetization transfer, T2* and B0 orientation to study the myelo-architecture of the in vivo human cortex. NeuroImage 119, 89–102. doi:10.1016/j.neuroimage.2015.06.033.

Marques, J.P., Khabipova, D., Gruetter, R., 2017. Studying cyto and myeloarchitecture of the human cortex at ultra-high field with quantitative imaging: R1, R2* and magnetic susceptibility. NeuroImage 147 (December 2016), 152–163. doi:10.1016/j.neuroimage.2016.12.009.

Marques, J.P., Kober, T., Krueger, G., van der Zwaag, W., Van de Moortele, P.F., Gruetter, R., et al., 2010. MP2RAGE, a self bias-field corrected sequence for improved segmentation and T1-mapping at high field. NeuroImage 49 (2), 1271–1281. doi:10.1016/j.neuroimage.2009.10.002.

Martin, W.R.W., Wieler, M., Gee, M., 2008. Midbrain iron content in early Parkinson disease: apotential biomarker of disease status. Neurology 70 (16 PART 2), 1411–1417. doi:10.1212/01.wnl.0000286384.31050.b5.

Metere, R., Möller, H.E., 2018. Quantifying the myelin and iron contents of the brain in vivo using a linear model of relaxation. Proc. Int. Soc. Magn. Reson. Med. 26, 5505.

Miletić, S., Bazin, P.-L., Weiskopf, N., van der Zwaag, W., Forstmann, B.U., Trampel, R., et al., 2020. fMRI protocol optimization for simultaneously studying small subcortical and cortical areas at 7 T. NeuroImage 219 (May). doi:10.1016/j.neuroimage.2020.116992.

Mink, J.W., 1996. The basal ganglia: focused selection and inhibition of competing motor programs. Prog. Neurobiol. 50 (4), 381–425. doi:10.1016/S0301-0082(96)00042-1.

Mulder, M.J., Keuken, M.C., Bazin, P.-l., Alkemade, A., Forstmann, B.U., et al., 2019. Size and shape matter: the impact of voxel geometry on the identification of small nuclei. PLoS One 14 (4), e0215382. doi:10.1371/journal.pone.0215382.

Narvacan, K., Treit, S., Camicioli, R., Martin, W., Beaulieu, C., et al., 2017. Evolution of deep gray matter volume across the human lifespan. Hum. Brain Mapp. 38 (8), 3771–3790. doi:10.1002/hbm.23604.

O'Doherty, J., Dayan, P., Schultz, J., Deichmann, R., Friston, K.J., Dolan, R.J., et al., 2004. Dissociable roles of ventral and dorsal striatum in instrumental conditioning. Science 304 (5669), 452–454. doi:10.1126/science.1094285.

Ogg, R.J., Steen, R.G., 1998. Age-related changes in brain T1 are correlated with iron concentration. Magn. Reson. Med. 40 (5), 749–753. doi:10.1002/mrm.1910400516.

Pauli, W.M., Nili, A.N., Tyszka, J.M., 2018. A high-resolution probabilistic in vivo atlas of human subcortical brain nuclei. Sci. Data 5 (1), 180063. doi:10.1038/sdata.2018.63.

Pham, D.L., Bazin, P.L., 2009. Unsupervised Tissue Classification, second ed. Elsevier Inc. doi:10.1016/B978-012373904-9.50020-9.

Potvin, O., Mouiha, A., Dieumegarde, L., Duchesne, S., et al., 2016. Normative data for subcortical regional volumes over the lifetime of the adult human brain. NeuroImage 137, 9–20. doi:10.1016/j.neuroimage.2016.05.016.

Ramos, P., Santos, A., Pinto, N.R., Mendes, R., Magalhães, T., Almeida, A., et al., 2014. Iron levels in the human brain: a post-mortem study of anatomical region differences and age-related changes. J. Trace Elem. Med. Biol. 28 (1), 13–17. doi:10.1016/j.jtemb.2013.08.001.

Randall, L.O., 1938. Chemical topography of the brain. J. Biol. Chem. 124 (2), 481–488.

Rawlings, J.O., Pantula, S.G., Dickey, D.A., 1998. Applied Regression Analysis. Springer-Verlag, New York doi:10.1007/b98890.

Raz, N., 2004. The aging brain observed in vivo. In: Cognitive Neuroscience of Aging, vol. 15. Oxford University Press, pp. 19–57. doi:10.1093/acprof:oso/9780195156744.003.0002.

Raz, N., Lindenberger, U., Rodrigue, K.M., Kennedy, K.M., Head, D., Williamson, A., Dahle, C., Gerstorf, D., Acker, J.D., et al., 2005. Regional brain changes in aging healthy adults: general trends, individual differences and modifiers. Cereb. Cortex 15 (11), 1676–1689. doi:10.1093/cercor/bhi044.

Raz, N., Rodrigue, K.M., 2006. Differential aging of the brain: patterns, cognitive correlates and modifiers. Neurosci. Biobehav. Rev. 30 (6), 730–748. doi:10.1016/j.neubiorev.2006.07.001.

Raznahan, A., Shaw, P.W., Lerch, J.P., Clasen, L.S., Greenstein, D., Berman, R., Pipitone, J., Chakravarty, M.M., Giedd, J.N., et al., 2014. Longitudinal four-dimensional mapping of subcortical anatomy in human development. Proc. Natl. Acad. Sci. 111 (4), 1592–1597. doi:10.1073/pnas.1316911111.

Rooney, W.D., Johnson, G., Li, X., Cohen, E.R., Kim, S.-G., Ugurbil, K., Springer, C.S., 2007. Magnetic field and tissue dependencies of human brain longitudinal1H2O relaxation in vivo. Magn. Reson. Med. 57 (2), 308–318. doi:10.1002/mrm.21122.

Samanez-Larkin, G.R., D'Esposito, M., 2008. Group comparisons: imaging the aging brain. Soc. Cogn. Affect. Neurosci. 3 (3), 290–297. doi:10.1093/scan/nsn029.

Schenck, J.F., Zimmerman, E.A., 2004. High-field magnetic resonance imaging of brain iron: birth of a biomarker? NMR Biomed. 17 (7), 433–445. doi:10.1002/nbm.922.

Schmierer, K., Wheeler-Kingshott, C.A.M., Tozer, D.J., Boulby, P.A., Parkes, H.G., Yousry, T.A., Scaravilli, F., Barker, G.J., Tofts, P.S., Miller, D.H., et al., 2008. Quantitative magnetic resonance of postmortem multiple sclerosis brain before and after fixation. Magn. Reson. Med. 59 (2), 268–277. doi:10.1002/mrm.21487.

Schultz, W., Dayan, P., Montague, P.R., 1997. A neural substrate of prediction and reward. Science 275 (5306), 1593–1599. doi:10.1126/science.275.5306.1593.

Schwarz, G., 1978. Estimating the dimension of a model. Ann. Stat. 6 (2), 461–464. doi:10.1214/aos/1176344136.

Seabold, S., Perktold, J., 2010. Statsmodels: econometric and statistical modeling with Python. In: 9th Python in Science Conference, pp. 57–61.

Shen, S., Sandoval, J., Swiss, V.A., Li, J., Dupree, J., Franklin, R.J.M., Casaccia-Bonnefil, P., et al., 2008. Age-dependent epigenetic control of differentiation inhibitors is critical for remyelination efficiency. Nat. Neurosci. 11 (9), 1024–1034. doi:10.1038/nn.2172.

Shepherd, G.M.G., 2013. Corticostriatal connectivity and its role in disease. Nat. Rev. Neurosci. 14 (4), 278–291. doi:10.1038/nrn3469.

Shepherd, T.M., Flint, J.J., Thelwall, P.E., Stanisz, G.J., Mareci, T.H., Yachnis, A.T., Blackband, S.J., et al., 2009. Postmortem interval alters the water relaxation and diffusion properties of rat nervous tissue—Implications for MRI studies of human autopsy samples. NeuroImage 44 (3), 820–826. doi:10.1016/j.neuroimage.2008.09.054.

Stafford, J.L., Albert, M.S., Naeser, M.A., Sandor, T., Garvey, A.J., et al., 1988. Age-related differences in computed tomographic scan measurements. Arch. Neurol. 45 (4), 409–415. doi:10.1001/archneur.1988.00520280055016.

Steen, R.G., Reddick, W.E., Ogg, R.J., 2000. More than meets the eye: significant regional heterogeneity in human cortical T1. Magn. Reson. Imaging 18 (4), 361–368. doi:10.1016/S0730-725X(00)00123-5.

Stüber, C., Morawski, M., Schäfer, A., Labadie, C., Wähnert, M., Leuze, C., Streicher, M., Barapatre, N., Reimann, K., Geyer, S., Spemann, D., Turner, R., et al., 2014. Myelin and iron concentration in the human brain: quantitative study of MRI contrast. NeuroImage 93 (P1), 95–106. doi:10.1016/j.neuroimage.2014.02.026.

Sullivan, E.V., Rosenbloom, M., Serventi, K.L., Pfefferbaum, A., et al., 2004. Effects of age and sex on volumes of the thalamus, pons, and cortex. Neurobiol. Aging 25 (2), 185–192. doi:10.1016/S0197-4580(03)00044-7.

Tardif, C.L., Steele, C.J., Lampe, L., Bazin, P.L., Ragert, P., Villringer, A., Gauthier, C.J., et al., 2017. Investigation of the confounding effects of vasculature and metabolism on computational anatomy studies. NeuroImage 149 (September 2016), 233–243. doi:10.1016/j.neuroimage.2017.01.025.

Tian, Y., Margulies, D.S., Breakspear, M., Zalesky, A., et al., 2020. Topographic organization of the human subcortex unveiled with functional connectivity gradients. Nat. Neurosci. 23 (11), 1421–1432. doi:10.1038/s41593-020-00711-6.

Tovi, M., Ericsson, A., 1992. Measurements of T1 and T2 over time in formalin-fixed human whole-brain specimens. Acta Radiol. 33 (5), 400–404. doi:10.1080/02841859209172021.

Trutti, A.C., Fontanesi, L., Mulder, M.J., Bazin, P.-L., Hommel, B., Forstmann, B.U., et al., 2021. A probabilistic atlas of the human ventral tegmental area (VTA) based on 7 Tesla MRI data. Brain Struct. Funct. doi:10.1007/s00429-021-02231-w.

Tullo, S., Patel, R., Devenyi, G.A., Salaciak, A., Bedford, S.A., Farzin, S., Wlodarski, N., Tardif, C.L., Breitner, J.C.S., Chakravarty, M.M., et al., 2019. MR-based age-related effects on the striatum, globus pallidus, and thalamus in healthy individuals across the adult lifespan. Hum. Brain Mapp. 40 (18), 5269–5288. doi:10.1002/hbm.24771.

Turner, B.M., 2019. Toward a common representational framework for adaptation. Psychol. Rev. doi:10.1037/rev0000148.

Uddin, M.N., Figley, T.D., Marrie, R.A., Figley, C.R., et al., 2018. Can T1w/T2w ratio be used as a myelin-specific measure in subcortical structures? Comparisons between FSE-based T1w/T2w ratios, GRASE-based T1w/T2w ratios and multi-echo GRASE-based myelin water fractions. NMR Biomed. 31 (3), 1–11. doi:10.1002/nbm.3868.

Uddin, M.N., Figley, T.D., Solar, K.G., Shatil, A.S., Figley, C.R., et al., 2019. Comparisons between multi-component myelin water fraction, T1w/T2w ratio, and diffusion tensor imaging measures in healthy human brain structures. Sci. Rep. 9 (1), 1–17. doi:10.1038/s41598-019-39199-x.

Wagenmakers, E.-J., Farrell, S., 2004. AIC model selection using Akaike weights. Psychon. Bull. Rev. 11 (1), 192–196. doi:10.3758/BF03206482.

Walhovd, K.B., Fjell, A.M., Giedd, J., Dale, A.M., Brown, T.T., et al., 2016. Through thick and thin: a need to reconcile contradictory results on trajectories in human cortical development. Cereb. Cortex 27 (2), 1–10. doi:10.1093/cercor/bhv301.

Walhovd, K.B., Fjell, A.M., Reinvang, I., Lundervold, A., Dale, A.M., Eilertsen, D.E., Quinn, B.T., Salat, D., Makris, N., Fischl, B., et al., 2005. Effects of age on volumes of cortex, white matter and subcortical structures. Neurobiol. Aging 26 (9), 1261–1270. doi:10.1016/j.neurobiolaging.2005.05.020.

Walhovd, K.B., Westlye, L.T., Amlien, I., Espeseth, T., Reinvang, I., Raz, N., Agartz, I., Salat, D.H., Greve, D.N., Fischl, B., Dale, A.M., Fjell, A.M., et al., 2011. Consistent neuroanatomical age-related volume differences across multiple samples. Neurobiol. Aging 32 (5), 916–932. doi:10.1016/j.neurobiolaging.2009.05.013.

Wang, Q., Xu, X., Zhang, M., 2010. Normal aging in the basal ganglia evaluated by eigenvalues of diffusion tensor imaging. Am. J. Neuroradiol. 31 (3), 516–520. doi:10.3174/ajnr.A1862.

Wang, Y., Xu, Q., Luo, J., Hu, M., Zuo, C., et al., 2019. Effects of age and sex on subcortical volumes. Front. Aging Neurosci. 11 (SEP), 1–12. doi:10.3389/fnagi.2019.00259.

Ward, R.J., Zucca, F.A., Duyn, J.H., Crichton, R.R., Zecca, L., et al., 2014. The role of iron in brain ageing and neurodegenerative disorders. Lancet Neurol. 13 (10), 1045–1060. doi:10.1016/S1474-4422(14)70117-6.

Weiskopf, N., Mohammadi, S., Lutti, A., Callaghan, M.F., et al., 2015. Advances in MRI-based computational neuroanatomy: from morphometry to in-vivo histology. Curr. Opin. Neurol. 28 (4), 313–322. doi:10.1097/WCO.0000000000000222.

Ye, R., Rua, C., O'Callaghan, C., Jones, P.S., Hezemans, F.H., Kaalund, S.S., Tsvetanov, K.A., Rodgers, C.T., Williams, G., Passamonti, L., Rowe, J.B., et al., 2021. An in vivo probabilistic atlas of the human locus coeruleus at ultra-high field. NeuroImage 225 (October 2020), 117487. doi:10.1016/j.neuroimage.2020.117487.

Zecca, L., Youdim, M.B.H., Riederer, P., Connor, J.R., Crichton, R.R., et al., 2004. Iron, brain ageing and neurodegenerative disorders. Nat. Rev. Neurosci. 5 (11), 863–873. doi:10.1038/nrn1537.

Zhang, Y., Wei, H., Cronin, M.J., He, N., Yan, F., Liu, C., et al., 2018. Longitudinal data for magnetic susceptibility of normative human brain development and aging over the lifespan. Data Brief 20, 623–631. doi:10.1016/j.dib.2018.06.005.